

# Quadrupole collective states in a large single- $j$ shell

K. Burzyński<sup>1</sup> and J. Dobaczewski<sup>1,2</sup>

<sup>1</sup>*Institute of Theoretical Physics, Warsaw University, Hoża 69, PL-00-681 Warsaw, Poland*

<sup>2</sup>*University of Pittsburgh, Pittsburgh, PA 15260, USA*

## Abstract

We discuss the ability of the generator coordinate method (GCM) to select collective states in microscopic calculations. The model studied is a single- $j$  shell with hamiltonian containing the quadrupole-quadrupole interaction. Quadrupole collective excitations are constructed by means of the quadrupole single-particle operator. Lowest collective bands for  $j=31/2$  and particle numbers  $N=4,6,8,10,12$ , and 14 are found. For lower values of  $j$ , exact solutions are obtained and compared with the GCM results.

PACS Numbers 21.10Re, 21.60Ev

## I. INTRODUCTION

A microscopic description of nuclear collective modes is still a very important and interesting problem studied in the theory of nuclear structure. In a frame of the shell model such a description is difficult to obtain because of a very large size of the basis required to include all necessary configurations. For example, only very recently excellent shell-model results for rotational states in  $^{48}\text{Cr}$  have been obtained [1]. Although many phenomenological approaches can, and have been constructed, their microscopic derivation from the shell model is often not entirely accomplished. It is therefore important to analyze and study approaches which are able to provide a simultaneous description of collective and single-particle phenomena.

The generator coordinate method (GCM) [2–5] constitutes an effective method to deal with collective degrees of freedom while starting from a pure many-fermion description. Moreover, it may also yield an exact quantum mechanical formalism, and only the choice of generating functions and a generator coordinate decides whether we can find exact solutions, collective as well as noncollective, to the actual problem. The configuration mixing feature which is by construction built in into the GCM provides us with the ideal tool to study microscopic foundations of collective models.

In the present study, we apply the GCM to a microscopic model of a single- $j$  shell filled with even number of identical nucleons interacting via pairing-plus-quadrupole hamiltonian [6]. Although the model is very simple, it contains two main ingredients of the “real” nuclear structure theories, i.e., the quadrupole deformation and the pairing correlations, and at the same time for low values of  $j$  it is relatively easy to solve. On the other hand, the GCM is well suited to study this model for large values of  $j$  where the exact solutions are inaccessible.

In the past the single- $j$  shell model has been studied by many authors. Mulhall and Sips [7] found that even for 4 particles occupying single- $j$  shell with strong quadrupole-quadrupole force the collective effects are important and rotational structures are present in the spectra. Deformability, i.e., a competition between the quadrupole force and the pairing, was studied in a series of papers by Baranger and Kumar [8,9]. Arima [10] discussed excited rotational level structures ( $K=2$  bands) appearing in the single- $j$  shell. Friedman and Kelson [11] analyzed collective spectra as depending on particle number and  $j$ . The present paper aims at using the GCM as a filter which would select collective structures among the complete shell-model spectrum. Such a study may give us more confidence in using the GCM in more realistic cases where the quality of approximations involved is difficult to analyze.

The paper is organized in the following way: In Sec. II we fix notation by briefly reviewing the pairing-plus-quadrupole model in a single- $j$  shell and then in Sec. II A we present the available exact solutions. The key point of the GCM is the construction of the generating states, which we present in Sec. II B by invoking the single particle coherent excitation model (SCEM) of Dobaczewski and Rohoziński [12,13]. In this model the quadrupole excitations are build using the single-particle quadrupole operator. In the present study we restore the broken particle-number and angular-momentum symmetries exactly. This is done in a consistent GCM framework by using the gauge angle and the Euler angles as generator coordinates. The particle-number projection [14,15] is based on the Fomenko method [16,17] in which integrals are replaced by finite sums, Sec. III A, and a similar method is also used to perform the angular momentum projection [18,19], Sec. III B. A description of the GCM

calculations in the intrinsic frame of reference is presented in Sec. IV. In Sec. IV A we analyze the GCM results for  $j=15/2$  and  $N=8$  particles and compare them with the exact calculations. In Sec. IV B we present the GCM spectra for  $j=31/2$  and  $N=4$ , and for particle numbers between 6 and 14, where the exact solutions are not available.

## II. SINGLE- $J$ SHELL

We consider the  $(2j+1)$ -fold degenerate single shell of angular momentum  $j$  filled with even number  $N$  of identical particles, which without the interaction is assumed to be at zero energy. The hamiltonian is composed of the pairing-plus-quadrupole interaction,

$$\hat{H} = -G\hat{P}^+\hat{P} - \chi\hat{Q}\cdot\hat{Q}, \quad (2.1)$$

where  $\hat{P}^+$  is the pair transfer operator and  $\hat{Q}$  is the quadrupole moment operator,

$$\hat{P}^+ = \sum_{mm'} (jmjm'|00)a_m^+a_{m'}^+, \quad (2.2a)$$

$$\hat{Q}_\mu^+ = \sum_{mm'} (jmjm'|2\mu)a_m^+\tilde{a}_{m'}^+, \quad (2.2b)$$

while  $G$  and  $\chi$  are pairing and quadrupole coupling constants, respectively. Hamiltonian (2.1) describes basic collective correlations between nucleons [6,7] and it has been used by many authors [8–11,20,21].

In the present paper we aim at solving the pairing-plus-quadrupole model in a large single- $j$  shell. Dimensions of the many-fermion space increase rapidly with  $j$  and the exact solutions become inaccessible very fast. For example, in the  $M$  and  $J$  representations the maximum dimensions for  $j=15/2$  are 526 and 35, respectively, while for  $j=31/2$  they are as large as 8 908 546 and 200 691. The generator coordinate method, which we apply in Sec. IV to this problem, is able to describe low lying collective states without using very large matrices. Here we present solutions for the values of particle number  $N$  and single-particle angular momentum  $j$  for which in the  $M$  representation the dimensions of the many-particle space are not larger than 5000.

### A. Exact diagonalization

In Fig. 1 we show the yrast bands for  $N=8$  particles in the  $j=15/2$  shell obtained with several values of the coupling constants  $G$  and  $\chi$ , see Eq. 2.1. Using the parametrizations  $G=(1-x)\times 1$  MeV and  $\chi=x\times 1$  MeV we show a transition from the pairing (seniority) limit at  $x=0$  to a large-deformation limit at  $x=1$ . It can be seen that for  $x<1$  the spectra are strongly influenced by the fixed-seniority structures which at  $x=0$  appear as degenerate multiplets. Since in this paper we want to discuss situations corresponding to collective quadrupole excitations, in the following we present only the results for the pure quadrupole-quadrupole force, i.e., we set  $G=0$  and  $\chi=1$  MeV.

In Fig. 2(a) we present the yrast bands for  $N=4$  particles interacting with the quadrupole-quadrupole interaction in shells corresponding to  $j$  between  $15/2$  and  $31/2$ . At low spins,

regular rotational-like bands are obtained with moments of inertia  $\mathcal{J}=3\hbar^2/E_{2+}$  varying between  $51 \hbar^2/\text{MeV}$  for  $j=15/2$  and  $333 \hbar^2/\text{MeV}$  for  $j=31/2$ , and the corresponding  $E_{4+}/E_{2+}$  ratios varying between 3.23 and 3.32 ( $E_{I+}$  denotes the excitation energy above the ground state).

At higher spins the ground-state bands are crossed by bands built on high- $K$  particle-hole excitations, which can easily be identified with oblate structures. In the Nilsson single-particle diagram presented in Fig. 3 for  $j=15/2$ , we see that at the oblate side the four particles occupy the  $\Omega=15/2$  and  $13/2$  orbitals. Therefore the lowest single-particle excitation corresponds to promoting a particle from  $\Omega=13/2$  to  $\Omega=11/2$  which gives the  $K=13/2+11/2=12$  excitation and leads to a band head at  $I=12$ . Similarly, for larger values of  $j$  one obtains band heads at larger even values of spin.

For  $N=6$  particles, Fig. 2(b), we see the bands which correspond to 2p-2h oblate configurations. For example, for  $j=21/2$  the p-h band corresponds to exciting the  $\Omega=17/2$  particle to the  $\Omega=15/2$  orbital ( $K=16$ ) and then the second p-h excitation aligns the  $\Omega=19/2$  particle to the  $\Omega=13/2$  orbital leading to  $K=32$  and giving the band head at  $I=32$ . We see that for small shell-filling factors  $N/(2j+1)$  the high- $K$  bands appear at very low energies, while they cease to be yrast for larger shell-filling factors. For example, for  $N=8$  and  $10$ , Figs. 2(c) and (d), no yrast high- $K$  bands are seen and only yrast-yrare band interaction is visible at  $I=12$  for the lowest  $j=19/2$  and  $N=8$  bands. In general, the yrast bands for half-filled shells present regular collective structures, although they do not have pure rotational character, for example,  $E_{4+}/E_{2+}=1.92$  for the  $j=N-1/2=15/2$  band. This is due to the  $\gamma$ -instability of the corresponding potential energy surface (PES), see Fig. 4(a).

The complete spectrum of 526 states for  $N=8$  particles in the  $j=15/2$  shell is presented in Fig. 5. The lines connect states with the largest E2 reduced matrix elements of the quadrupole operator. Only the stretched  $\Delta I=2$  matrix elements are considered. The lowest  $0^+$  state is connected to the  $2^+$  state with which it has the largest E2 matrix element. Then the first excited  $0^+$  state is connected to one of the remaining  $2^+$  states, and the procedure is continued for still higher  $0^+$  states. After that all remaining  $2^+$  states are considered to be the band heads. In the next step the  $2^+$  states are considered by order of increasing energy and connected to the  $4^+$  states. In this way all even spins are connected into bands and then the same procedure is repeated for odd spin values.

Several regular collective bands can be seen in Fig. 5. These will be used to discuss the ability of the GCM to select collective structures in the sea of all possible eigenstates, Sec. IV A. Here we only discuss a possible interpretation of lowest states in terms of the collective model. In Table I we present the reduced E2 matrix elements between five lowest  $0^+$  and  $2^+$  states. It can be seen that these matrix elements obey a strong selection rule related to the special symmetry of the half-filled shell. Indeed, the quadrupole operator (2.2b) is odd with respect to changing the creation operator into the annihilation operator and *vice versa*. Therefore, the quadrupole-quadrupole hamiltonian is invariant with respect to such a change and the spectra of systems containing  $N$  and  $2j+1-N$  particles are strictly identical. However, for a half-filled shell  $N$  is equal to  $2j+1-N$  and the above symmetry allows to attribute a new dichotomic quantum number to every eigenstate, while the quadrupole operator may only connect states with these quantum numbers being different.

An approximate interpretation of the lowest states can be done in terms of the collective Jean-Wilets model [22], which describes collective states for the  $\gamma$ -unstable PES. In this

model the lowest-order quadrupole transition operator changes the seniority quantum number by one and therefore the parity of the seniority can be associated with the dichotomic quantum number discussed above. In this way the  $0_1^+$  and  $0_2^+$  states can be identified with seniority zero and three and the three lowest  $2^+$  states with seniority one, two, and four. In this scheme the states  $0_3^+$  and  $0_4^+$  can be interpreted as mixtures of the seniority six states with the seniority zero  $\beta$  vibrations, and the states  $2_4^+$  and  $2_5^+$  as mixtures of seniority five and seven with seniority one  $\beta$  vibrations. This interpretation is however not manifested in the energy spectra, where the characteristic Jean-Wilets multiplets are strongly split. One can also note that if the identification of the  $\beta$  vibrations is correct, the corresponding energy is rather high as compared to the energy of the motion in the  $\gamma$  direction. This high energy may also suggest that the collective  $\gamma$  vibrations are here directly mixed to non-collective states and that the  $\beta$  vibrations are absent in the model.

The first excited band can be interpreted as the  $\gamma$  vibration strongly coupled to rotations due to the  $\gamma$ -instability of the corresponding PES, Fig. 4(a). At spin  $I=8$  it is perturbed by a coupling to the lowest noncollective excitation promoting the  $\Omega=7/2$  particle to the  $\Omega=9/2$  state (if one considers the oblate side of the Nilsson diagram, Fig. 3). However, one is here unable to distinguish between the oblate and prolate structures, because the prolate side suggests an excitation of the  $\Omega=9/2$  particle to the  $\Omega=7/2$  state, which gives the same value of spin  $I=8$ .

For  $j=31/2$  the exact solutions are available for  $N=4$  only, Fig. 6. The collective bands are identified by the same procedure as described above using the reduced matrix elements of the quadrupole operator. At low spins one can see several regular bands which can be fairly well interpreted in terms of the  $\gamma$  vibrations coupled to an axial rotor with  $K$  being approximately a good quantum number. In this interpretation, the ground-state band is the  $K=0$  and  $n_\gamma=0$  band and the first excited band has  $K=2$  and  $n_\gamma=1$ . Then come two  $n_\gamma=2$  bands with  $K=4$  and  $K=0$  followed by two  $n_\gamma=3$  bands with  $K=6$  and  $K=2$ . One may even identify three  $n_\gamma=4$  bands with  $K=8, 4,$  and  $0$ . Again, in this interpretation there is no room for the  $\beta$  vibrations at low energies [23]. Table II shows the E2 reduced matrix elements between the lowest  $0^+$  and  $2^+$  states and confirms the above interpretation. A clear decrease of the matrix elements with the difference in the number of  $\gamma$ -vibrational quanta is manifest, however, the strict  $|\Delta n_\gamma| \leq 1$  selection rule is not present.

Similarly as for the yrast bands, Fig. 2, one may easily recognize in the spectrum of Fig. 6 the bands built on the oblate particle-hole excitations. Together with the excitation of the  $\Omega=29/2$  particle to the  $\Omega=27/2$  orbital, which becomes yrast at  $I=28$ , one can also identify the excitations of the same particle to the  $\Omega=25/2, 23/2, 21/2,$  and  $19/2$  orbitals. One may clearly see the effect of decreasing E2 probability when the band terminates; the band heads are then coupled stronger to adjacent bands than to the next members of the given band.

## B. The SCEM model in a single- $j$ shell

The single-particle coherent excitation model (SCEM) proposed by Dobaczewski and Rohoziński [12,13] is based on the assumption that the quadrupole excitations can be constructed by acting with the quadrupole fermion operator  $\hat{F}^+$  on a reference state of the form

$$|\text{ref}\rangle = (\hat{S}^+)^{N/2} |0\rangle, \quad (2.3)$$

i.e.,

$$|\Psi_{\text{SCEM}}\rangle = (\hat{F}^+)^{N_F} |\text{ref}\rangle, \quad (2.4)$$

where  $\hat{S}^+$  creates a monopole collective pair of particles and  $\hat{F}_\mu^+$  is a single-particle quadrupole excitation operator. Since only one operator of a given multipolarity can be constructed in the single- $j$  shell, here  $\hat{S}^+ \equiv \hat{P}^+$  and  $\hat{F}^+ \equiv \hat{Q}$ . In the SCEM, for  $N_F=0$  we obtain one state of  $I=0$  and for  $N_F=1$  one state of  $I=2$ . If for every value of  $N_F$  we orthogonalize the SCEM states with respect to those obtained for  $N_F-1$ , we obtain the numbers of states listed in Table III for  $j=15/2$  and  $N=8$ .

It can be seen that for low values of  $N_F$  the numbers of states of a given  $I$  exactly correspond to those of the five-dimensional harmonic oscillator [24] with  $N_F$  phonons, or to the numbers of  $d^+$ s excitations required to create the interacting-boson-model states [25] from the s-boson condensate  $(s^+)^{N_F}$ . However, SCEM being a true fermion model, there are departures from this rule appearing as soon as  $N_F$  reaches half of the shell's maximum particle number  $j+1/2$  (i.e., in Table III from  $N_F=4$  on), which reflect the effect of the Pauli correlations. It is obvious that states of the angular momentum  $I$  can only be obtained for  $N_F \geq I/2$  and therefore the number of excitations  $N_F$  plays the role of the cut-off in spin.

The generating function of the GCM is here constructed as a condensate of the  $\hat{F}^+$  excitations acting on a condensate of the  $\hat{S}^+$  pairs

$$|t_0 t_2\rangle = \exp(t_2 \cdot \hat{F}^+) \exp(t_0 \hat{S}^+) |0\rangle. \quad (2.5)$$

The parameters  $t_0$  and  $t_2$  are a scalar and a quadrupole numerical tensors, respectively, and are used as the generator coordinates. We use the notation of the scalar product defined as  $t_2 \cdot \hat{F}^+ = \sum_\mu t_{2\mu}^* \hat{F}_\mu^+$  and assume that  $t_{2\mu}^* = (-1)^\mu t_{2,-\mu}$  and  $t_0 = t_0^*$ .

For the GCM state (2.5) neither the particle number nor the angular momentum is a good quantum number. It can, however, be decomposed into the SCEM states (2.4) which, with a proper angular momentum coupling of the excitation operators  $\hat{F}^+$ , have good angular momentum and particle number. The average value of the particle number in the generating function (2.5) increases with the  $t_0$  parameter. Similarly, the average number of the excitations  $\hat{F}^+$ , and hence the average value of the angular momentum, increases with the magnitude of the quadrupole tensor [26]

$$\beta^2 = \sum_\mu |t_{2\mu}|^2. \quad (2.6)$$

It is convenient to introduce three matrices

$$S_{mm'}^+ = (jmjm'|00) = (-1)^{j-m} \frac{1}{\sqrt{2j+1}} \delta_{m,-m'}, \quad (2.7a)$$

$$F_{mm'}^{\mu+} = (jmj-m'|2\mu) (-1)^{j+m'}, \quad (2.7b)$$

$$F_{mm'}^+ = \sum_\mu t_{2\mu}^* F_{mm'}^{\mu+}, \quad (2.7c)$$

where  $S$  is antisymmetric and  $F$  is hermitian, in terms of which the basic SCEM building blocks read

$$\hat{S}^+ = \sum_{mm'} S_{mm'} a_m^+ a_{m'}^+ , \quad (2.8a)$$

$$\hat{F}_\mu^+ = \sum_{mm'} F_{mm'}^{\mu+} a_m^+ a_{m'}^+ , \quad (2.8b)$$

$$t_2 \cdot \hat{F}^+ = \sum_{mm'} F_{mm'} a_m^+ a_{m'}^+ . \quad (2.8c)$$

Now, the generating function (2.5) can be represented as

$$|t_0 t_2\rangle = \exp(t_0 e^{t_2 \cdot \hat{F}^+} \hat{S}^+ e^{-t_2 \cdot \hat{F}^+}) |0\rangle , \quad (2.9)$$

and further, using the nonunitary Bogoliubov transformation [27], as a Thouless [28] state:

$$|t_0 t_2\rangle = \exp\left(\frac{1}{2} \sum_{mm'} C_{mm'}^+ a_m^+ a_{m'}^+\right) |0\rangle , \quad (2.10)$$

where

$$C_{mm'}^+ = 2t_0 \sum_{nn'} (e^F)_{mn} S_{nn'}^+ (e^{F^*})_{n'm'} . \quad (2.11)$$

In this way all GCM kernels can be easily calculated using the standard expressions resulting from the Wick theorem [29,5]. On the other hand, the product of matrices in (2.11) can be rapidly obtained by using the  $F$  matrix in its eigen-reference-frame, which corresponds to transforming the tensor  $t_2$  to the intrinsic system defined by conditions

$$t_{21} = 0 , \quad t_{22} = t_{22}^* , \quad (2.12)$$

and then diagonalizing the mean field  $F$  in the intrinsic frame. In cases when the  $\hat{S}^+$  pair has the seniority form, i.e., contains pairs of time-reversed states with equal amplitudes as is in the single- $j$  shell (2.7a), we may further simplify expression (2.11) by using the fact that  $F$  is a time-even matrix, i.e.,

$$C_{mm'}^+ = \frac{2t_0 (-1)^{j+m'}}{\sqrt{2j+1}} (e^{2F})_{m,-m'} . \quad (2.13)$$

### III. RESTORATION OF BROKEN SYMMETRIES

It is well known that the GCM for the gauge angle and the Euler angles used as generator coordinates is equivalent to the exact particle-number and angular-momentum projections [30,4,5]. In the present study we use this property to restore those broken symmetries exactly, and then the GCM equation is solved in the intrinsic frame of reference.

### A. Particle-number projection

A standard way [14,15,31,5] to perform the particle-number projection is to introduce a gauge angle and to integrate over its  $(0, 2\pi)$  domain. Using the generating function in the form (2.10), the projected state is

$$|Nt_2\rangle \equiv \hat{P}_N|t_0t_2\rangle = \frac{1}{2\pi} \int_0^{2\pi} d\phi e^{-iN\phi} \exp\left(\frac{1}{2} \sum_{mm'} C_{mm'}^+ e^{2i\phi} a_m^+ a_{m'}^+\right) |0\rangle. \quad (3.1)$$

Such an integration leaves only the components of the wave function with the particle number  $N$ . This is based on the following orthogonality relation valid for any integer  $N$  and  $N'$

$$\frac{1}{2\pi} \int_0^{2\pi} d\phi e^{i(N'-N)\phi} = \delta_{NN'}. \quad (3.2)$$

When calculating matrix elements of any arbitrary particle-number-conserving operator  $\hat{O}$  between the Thouless states, the integration over the gauge angle can be done only for one of those states

$$\langle Nt_2|\hat{O}|Nt'_2\rangle \equiv \langle t_0t_2|\hat{O}\hat{P}_N|t'_0t'_2\rangle = \frac{1}{2\pi} \int_0^{2\pi} d\phi e^{-iN\phi} \langle t_0t_2|\hat{O}|e^{2i\phi}t'_0, t'_2\rangle, \quad (3.3)$$

which amounts to multiplying the Thouless matrix  $C'$  (or, in other words, the coefficient  $t'_0$ ) of the ket state by the factor  $e^{2i\phi}$  and integrating over  $\phi$ .

When there is an upper limit  $N_{\max}$  on the particle number of the system, as is the case in the single- $j$  shell, the integral (3.3) can be discretized as proposed by Fomenko [16,17]. Instead of Eq. (3.2) one can write

$$\frac{1}{N_{\max} + 1} \sum_{n=0}^{N_{\max}} e^{i(N'-N)n\Delta\phi} = \begin{cases} 1 & \text{for } N' = N \\ \frac{1}{N_{\max} + 1} \frac{1 - \exp[i(N' - N)(N_{\max} + 1)\Delta\phi]}{1 - \exp[i(N' - N)\Delta\phi]} & \text{for } N' \neq N \end{cases}. \quad (3.4)$$

Taking  $\Delta\phi=2\pi/(N_{\max}+1)$ , the numerator of the expression for  $N' \neq N$  vanishes for all  $N$  and  $N'$ , whereas the denominator does not vanish for any  $N$  and  $N'$  not larger than  $N_{\max}$ , i.e.,

$$\frac{1}{N_{\max} + 1} \sum_{n=0}^{N_{\max}} e^{i(N'-N)n\Delta\phi} = \delta_{NN'} \quad \text{for } N, N' \leq N_{\max}. \quad (3.5)$$

For systems with even particle numbers we may repeat a similar discretization using only  $\frac{1}{2}N_{\max}$  points and  $\Delta'\phi=\pi/(\frac{1}{2}N_{\max}+1)$ , which gives

$$\frac{1}{\frac{1}{2}N_{\max} + 1} \sum_{n=0}^{\frac{1}{2}N_{\max}} e^{i(N'-N)n\Delta'\phi} = \delta_{NN'} \quad \text{for even } N, N' \leq N_{\max}. \quad (3.6)$$

Furthermore, assuming that  $\frac{1}{2}N_{\max}$  is also even, or proceeding as if  $N_{\max}$  was larger by 2 when  $\frac{1}{2}N_{\max}$  is odd, the left hand side of Eq. (3.6) can be rewritten in a form of the sum over  $n$  from  $-\frac{1}{4}N_{\max}$  to  $\frac{1}{4}N_{\max}$ , and finally



$$\frac{2}{\frac{1}{2}N_{\max} + 1} \left[ \frac{1}{2} + \Re \sum_{n=1}^{\frac{1}{4}N_{\max}} e^{i(N'-N)n\Delta'\phi} \right] = \delta_{NN'} \quad \text{for even } N, N' \leq N_{\max}. \quad (3.7)$$

Since the unprojected GCM states are time-even, the matrix elements of time-even operators are real and then the prescription for the projected matrix elements takes the following form

$$\langle Nt_2 | \hat{O} | Nt'_2 \rangle = \frac{2}{\frac{1}{2}N_{\max} + 1} \left[ \frac{1}{2} \langle t_0 t_2 | \hat{O} | t'_0 t'_2 \rangle + \Re \sum_{n=1}^{\frac{1}{4}N_{\max}} e^{-iNn\Delta'\phi} \langle t_0 t_2 | \hat{O} | e^{2in\Delta'\phi} t'_0, t'_2 \rangle \right], \quad (3.8)$$

where only  $\frac{1}{4}N_{\max}$  integration points are required.

The standard formulas resulting from the Wick [29,5] and Thouless [28,5] theorems applied to evaluate  $\langle t_0 t_2 | \hat{O} | e^{2in\Delta'\phi} t'_0, t'_2 \rangle$  matrix elements contain the products of matrices  $C^+ C'$ , cf. Eq. (2.10). Since using the projection method requires many such matrix multiplications a very efficient algorithm can be obtained by transforming  $C^+ C'$  to the basis in which it is diagonal (Appendix A). Then the matrix multiplications reduce to simple sums and products of the corresponding eigenvalues. At the same time the sign problem of the GCM kernels is avoided by considering only one half of pairwise degenerate eigenvalues [32].

## B. Angular-momentum projection

The practical techniques of the exact angular momentum projection were discussed many times in the literature [33,34]. We review here the formalism in the form suitable for the description of the quadrupole degrees of freedom.

Let us denote by  $|N\beta\gamma\rangle$  the particle-number-projected states (3.1) in the intrinsic frame defined by Eq. (2.12), where  $\beta$  and  $\gamma$  are the axial coordinates on the  $t_{20}$ - $t_{22}$  plane

$$t_{20} = \beta \cos \gamma, \quad \sqrt{2}t_{22} = \beta \sin \gamma. \quad (3.9)$$

According to standard prescriptions [5,18,19,30,31], the angular-momentum-projected GCM state  $|nNIM\rangle$  has the form

$$|nNIM\rangle = \sum_{K \geq 0} \int d\beta d\gamma \frac{g_{nIK}(\beta, \gamma)}{1 + \delta_{K0}} |NIMK\beta\gamma\rangle, \quad (3.10)$$

where the angular-momentum-projected intrinsic state  $|NIMK\beta\gamma\rangle$  is given by

$$|NIMK\beta\gamma\rangle = \frac{2I+1}{8\pi^2} \int d\Omega \left[ D_{MK}^{I*}(\Omega) + (-1)^I D_{M,-K}^{I*}(\Omega) \right] \hat{R}(\Omega) |N\beta\gamma\rangle. \quad (3.11)$$

The rotation operator  $\hat{R}(\Omega)$  depends on the three Euler angles,  $\Omega \equiv \phi, \theta, \psi$ . Due to the  $D_2$  symmetry of the GCM states (2.5) the sum in Eq. (3.10) is restricted to non-negative even values of  $K$ . Using states (3.10) one obtains the GCM (Hill-Wheeler) equation in the form [2,3,35]

$$\sum_{K' \geq 0} \int d\beta' d\gamma' \left[ \mathcal{H}_{KK'}^I(\beta, \gamma; \beta', \gamma') - E_n^I \mathcal{N}_{KK'}^I(\beta, \gamma; \beta', \gamma') \right] g_{nIK}(\beta, \gamma) = 0, \quad (3.12)$$

where  $\mathcal{H}$  and  $\mathcal{N}$  are the GCM kernel matrices of the hamiltonian and of the norm, respectively, defined as

$$\begin{aligned} \mathcal{O}_{KK'}^I(\beta, \gamma; \beta', \gamma') &= \frac{2I+1}{8\pi^2} \Delta_{KK'} \int d\Omega \langle N\beta\gamma | \hat{O}\hat{R}(\Omega) | N\beta'\gamma' \rangle \\ &\times \left[ D_{KK'}^{I*}(\Omega) + D_{-K-K'}^{I*}(\Omega) + (-1)^I D_{K-K'}^{I*}(\Omega) + (-1)^I D_{-KK'}^{I*}(\Omega) \right], \end{aligned} \quad (3.13)$$

and  $\Delta_{KK'}$  stands for  $1/((1+\delta_{K0})(1+\delta_{K'0}))$ . Since evaluation of kernels in Eq. (3.13) requires three dimensional integration, this is the most time consuming part of the numerical calculation.

Because all indices  $K$  and  $K'$  are even, we may use the explicit form [36] of the Wigner matrices,  $D_{KK'}^I(\Omega) = e^{iK\phi} d_{KK'}^I(\theta) e^{iK'\psi}$  to rewrite (3.13) in the following way

$$\begin{aligned} \mathcal{O}_{KK'}^I(\beta, \gamma; \beta', \gamma') &= 2 \frac{2I+1}{8\pi^2} \Delta_{KK'} \int_0^{2\pi} d\phi \int_0^\pi d\theta \sin\theta \int_0^{2\pi} d\psi \langle N\beta\gamma | \hat{O}\hat{R}(\phi, \theta, \psi) | N\beta'\gamma' \rangle \\ &\times \left[ d_{KK'}^I(\theta) \cos(K\phi + K'\psi) + (-1)^I d_{K-K'}^I(\theta) \cos(K\phi - K'\psi) \right]. \end{aligned} \quad (3.14)$$

By the same token the integration intervals over  $\phi$  and  $\psi$  can be reduced from  $(0, 2\pi)$  to  $(0, \pi)$ . Moreover, the Wigner functions  $d_{KK'}^I(\theta)$  depend then on  $x = \cos\theta$  only, and the integral  $\int_0^\pi d\theta \sin\theta$  can be rewritten as  $\int_{-1}^1 dx$ . Furthermore, symmetry properties [36] of  $d_{KK'}^I(\theta)$  allow also to reduce integration over  $x$  to the interval  $(0, 1)$ . Finally, the integration domain in (3.14) is eight times smaller and the factor 2 in front is replaced by 16.

Numerical integration over  $\phi$  and  $\psi$  Euler angles is done by means of the Tchebyshev method [37], i.e., values of the integrand in equally spaced points are summed up with equal weights. This method is exact when number of points is taken to be  $I_{\max}+1$ , where  $I_{\max}$  is the maximum spin of the good-angular-momentum components in the intrinsic state  $|N\beta\gamma\rangle$ . Integration over  $x$  is done using the Gauss-Legendre method [37] applied to the  $(0, 1)$  interval. Again, exact result is obtained by setting the number of points to  $I_{\max}+1$ .

#### IV. GCM CALCULATIONS IN THE INTRINSIC FRAME

The exact particle-number and angular-momentum projections allow us to calculate hamiltonian and norm kernels,  $\mathcal{H}_{KK'}^I(\beta, \gamma; \beta', \gamma')$  and  $\mathcal{N}_{KK'}^I(\beta, \gamma; \beta', \gamma')$ , for arbitrary pairs of intrinsic deformations  $(\beta, \gamma)$  and  $(\beta', \gamma')$ , which define the GCM equation (3.12). By a discretization of the  $\beta$  and  $\gamma$  variables this integral eigen-equation is transformed into a matrix eigen-equation, for which the kernels have to be calculated between all pairs of selected points  $(\beta_n, \gamma_n)$ ,  $n=1, \dots, N_d$ .

In principle, the invariant measure  $\beta^4 |\sin 3\gamma| d\beta d\gamma$  should be used in the GCM equation (3.12) for quadrupole motion. However, since we discretize this integral equation, the integration measure is immaterial. Moreover, we may then also include points for axial ( $\gamma=0$ ) and spherical ( $\beta=0$ ) shapes, which in the discretized GCM equation represent a certain volume of the phase space around points for which the invariant measure vanishes.

For a given  $j$ , the main factor determining the total computing time is the number  $N_d$  of the mesh points  $(\beta_n, \gamma_n)$  on the  $\beta$ - $\gamma$  plane, because the number of projected kernels

to be calculated is equal  $\frac{1}{2}N_d(N_d + 1)$ . Each of these kernels requires calculating  $(I_{\max}+1)^3$  overlaps for different Euler angles, Eq. (3.14). In Fig. 7 we present the CPU times required to calculate one hundred of such overlaps as a function of the single-particle angular momentum  $j$  of the shell. Full circles denote results obtained on a 50MHz PC-486 scalar computer. This computing time grows roughly as a third-order polynomial in  $j$  (solid line), which is a much slower increase than what would be required for an exact solution. The times obtained on a vector supercomputer CRAY Y/MP EL98 are marked with full squares. They were multiplied by a factor of 20 before plotting them together with the PC results. The increase of time with  $j$  is here much slower, which is due to a better performance of the vector processor obtained for larger matrices. In fact, this time can be approximated by a polynomial of a second degree in  $j$  (solid line).

In the present study we have performed the GCM calculations for  $j=31/2$  and for  $j=15/2$ . For the latter value, the exact results can easily be obtained and were used to test the GCM method.

As discussed in Sec. II B, the average value of angular momentum in the intrinsic states  $|N\beta\gamma\rangle$  increases with  $\beta$ . Similarly, for large values of  $I$  the collective weight functions  $g_{nIK}(\beta, \gamma)$  have large components at large  $\beta$ . Choosing the mesh of points  $(\beta_n, \gamma_n)$  with  $\beta_n$  smaller than a given value  $\beta_{\max}$  is equivalent to restricting the variational space to the values of spins smaller than a certain maximum value  $I_{\max}$ . In calculations we used  $\beta_{\max}=6$  which allows to properly describe spins up to  $I_{\max}=18$ .

Two meshes of points  $(\beta_n, \gamma_n)$  were used. The first one was composed of 10 points uniformly distributed in the sector  $\beta \leq \beta_{\max}$ ,  $0 \leq \gamma \leq 60^\circ$  (Fig. 4, full circles) in such a way that overlaps of the neighboring points do not differ too much one from another. The average overlap turns out to be 0.73 for  $N=10$  particles in the  $j=31/2$  shell and 0.80 for  $N=8$  and  $j=15/2$ . To test the influence of the number of points on the results, the second mesh comprising 19 points was constructed by adding one point in the middle of each triangle formed by three neighboring points of the 10-point lattice.

In Fig. 4 the PES in the intrinsic frame of reference is presented for the pure quadrupole force. The upper part shows the results for  $N=8$  and  $j = 15/2$ , in which case the PES has a deformed  $\gamma$ -unstable valley. Two absolute minima are at  $\beta \sim 3.5$  for  $\gamma=0^\circ$  and  $\gamma=60^\circ$  with a low saddle in between. The lower part of Fig. 4 shows the PES for  $N=10$  and  $j=31/2$ . In this case there appears a strongly pronounced oblate valley that extends towards large values of  $\beta$ .

The quadrupole moment of the intrinsic state can be calculated as an expectation value of the quadrupole operator in that state,

$$Q_\mu(\beta, \gamma) = \langle N\beta\gamma | \hat{Q}_\mu | N\beta\gamma \rangle . \quad (4.1)$$

The intrinsic frames of reference for the deformation tensor  $t_2$  and for the quadrupole tensor  $Q$  coincide, i.e., the only non-zero components of  $Q$  are

$$Q_0 = Q \cos \delta \quad \text{and} \quad \sqrt{2}Q_2 = Q \sin \delta , \quad (4.2)$$

which defines the radial coordinates in the  $Q$ - $\delta$  plane, in analogy to Eq. (3.9). When the mesh points of Fig. 4 are plotted in the  $Q$ - $\delta$  variables they appear to be distributed in a more uniform way than in the  $\beta$ - $\gamma$  variables. On the other hand, the topology of the PES

is the same in both representations, with one important difference, namely, due to a finite dimension of the single- $j$ -shell space, the quadrupole moment  $Q$  has its upper limit  $Q_{\max}$ . In Table IV the values of  $Q_{\max}$  are shown for several particle numbers in the  $j=15/2$  and  $j=31/2$  shells.

For  $j=31/2$  the intrinsic states  $|N\beta\gamma\rangle$  with the  $\beta$  coordinates beyond  $\beta\approx 10$  all have quadrupole moments close to the maximum value  $Q_{\max}$ . This means that there is no reason to extend the generating coordinates outside the  $\beta_{\max}=10$  circle, and in fact the value of  $\beta_{\max}=6$  used in the calculations is sufficient.

### A. GCM solutions for $j=15/2$ and $N=8$

In this section we present the GCM calculations for  $j=15/2$  and  $N=8$ , where the exact solutions are available and can be used to test the properties of the GCM approach. The Hill-Wheeler equation (3.12) is solved by using the standard method of calculating the square root of the overlap matrix  $\mathcal{N}_{KK'}^I$ , described in Ref. [5]. In what follows we compare the results obtained for 10 and 19 mesh points of intrinsic deformations, as defined in Sec. IV.

As is well known, the GCM overlap matrix has the spectrum with the zero value as an accumulating point, cf. the discussion in Ref. [38]. In principle this matrix is strictly positive definite but in practical calculations the negative eigenvalues may appear at the level of the numerical precision. This may be related to a finite precision of the diagonalization method, and especially to the numerical noise which may appear in calculating the elements of the overlap matrix. In Figs. 8(a) and 8(b) we present the absolute values of the overlap matrix for  $I=0$  and  $I=6$ , respectively, obtained with 19 mesh points. For  $I=0$  the exact spectrum contains 7 states, see Fig. 5 or Table V, and the overlap matrix has the same number of large eigenvalues separated by 10 orders of magnitude from the remaining 12 eigenvalues which represent the numerical noise. This illustrates a rare situation when the GCM generating functions exhaust the corresponding Hilbert space completely.

A more typical spectrum of the overlap matrix appears for  $I=6$ , where the total number of eigenvalues equals to 76 (its dimension equals the product of the number of points (19) and of the number of  $K$  components (4),  $K=0,2,4$ , and 6). Even if this dimension is larger than the number of the exact  $I=6$  states (31), the GCM generating functions do not exhaust the Hilbert space and no gap in the overlap spectrum occurs. In calculating the square root of the overlap one has to decide how many norm eigenvalues should be retained. Since the negative eigenvalues reflect the appearance of the numerical noise, their magnitude can be used as an indication of how much the results are perturbed by numerical uncertainties. Therefore, in the following we shall use and discuss a useful parameter denoted by  $k_{\text{crit}}$ , which is equal to the number of norm eigenvalues larger than the absolute value of the smallest eigenvalue. In Fig. 8 we present a graphic illustration of how this parameter is defined.

Let us denote by  $k$  the number of norm eigenvalues retained in solving the GCM equation. A choice of a proper value of  $k$  should be based on studying the stability of solutions when this parameter increases. In Fig. 9 we show the GCM energies for  $I=0$  (full circles) obtained by using 10 (a) and 19 (b) mesh points. The exact energies are also shown (open squares) and placed between the results obtained with  $k=k_{\text{crit}}$  and  $k=k_{\text{crit}}+1$ . It can be seen that the GCM calculation with  $k=7$  give the exact spectrum with a very good accuracy. This is

due to the fact that the complete Hilbert space is obtained in this case. For values of  $k=1,2$ , or 3 one obtains a fair description of 1,2, or 3 lowest states. On the other hand, the fourth state which first appears for  $k=4$  is correctly split into two exact solutions only after all the 7 basis states are included. We may see this kind of effect in many other examples and one may interpret it as a manifestation of the coupling of collective and non-collective degrees of freedom. Within this interpretation, for  $k=4$  the GCM correctly singles out the fourth collective state, which in reality is fragmented among the fourth and the fifth exact states.

As soon as we include in the basis more states than the critical value  $k_{\text{crit}}$ , there appear in the spectrum spurious states which have nothing in common with the exact solutions. Such states appear in an unpredictable way at various energies and in realistic calculations cannot be distinguished from the real ones. In fact, they also pollute the wave functions of states which have energies seemingly stable when  $k$  increases beyond the value of  $k_{\text{crit}}$ . Therefore, one should always try to avoid using too large values of  $k$  and an identification of a highest acceptable value is essential [39].

In Fig. 10 we present similar results for the  $I=2$  states. For both mesh sizes we obtain a good description of the four lowest states by using  $k=4$ . At higher energy one may identify two other structures which appear at  $k=5$  and  $k=9$ , and for increasing  $k$  become fragmented. For the 10-point calculation, except of the four lowest states, none of the higher excited states is reproduced with  $k \leq k_{\text{crit}}=12$ . On the other hand, for the 19-point mesh the exact spectrum is obtained for  $k \leq k_{\text{crit}}=16$ , because the full Hilbert space is then again exhausted by the GCM generating functions. It is interesting to note that for 10 mesh points the fifth exact state appears only beyond the value of  $k=k_{\text{crit}}$ . This may illustrate an approximate character of our prescription to define the critical value  $k_{\text{crit}}$ . For 19 points the fifth state is stable already at  $k=k_{\text{crit}}-2$ .

Based on this results we will suppose in what follows that using a relatively small number of mesh points of the intrinsic deformations (as compared to the number of exact states), one obtains a fair description of the collective subspace, and that only states with strong collective components are then present in the GCM spectra. By increasing the number of mesh points one includes noncollective configurations and the GCM yields collective states mixed with the noncollective ones. A separation of states into the collective and noncollective subspace is of course not a well defined procedure (both in the experiment and in the exactly solvable model discussed here). Which states are called collective is therefore a subject of a model interpretation. With increasing excitation energy the collectivity is gradually lost and the mixing with noncollective states increases. We may see, however, that the GCM can be used as a practical tool to select and decouple the collective space.

In Fig. 11 we compare the GCM spectra for spins up to  $I=6$  with the exact results. Again, both the 10-point (a) and 19-point (b) results are shown. In the GCM calculations the cut-off parameters  $k$  were chosen to be equal to the critical values  $k_{\text{crit}}$ , which are listed in Table V together with the corresponding numbers of exact states for a given spin. In all cases we have checked that the GCM states have correct average values of spin  $\langle \hat{I}^2 \rangle$  and particle numbers,  $\langle \hat{N} \rangle$  and  $\langle \hat{N}^2 \rangle$ , and that the average values of the hamiltonian  $\langle \hat{H} \rangle$  are equal to the GCM eigenenergies. These turn out to be useful criteria of identifying spurious states, because as soon as the spurious states start mixing with the physical ones the above average values become perturbed, even if the symmetries have been exactly restored when

calculating the GCM kernels.

In the GCM spectra there is no  $1^+$  states because they belong to representations of the point group  $D_2$  which are not included in the present calculations. Our choice of the generating functions (2.5) restricts them to the symmetric representation  $(+++)$  [24], and therefore such is the symmetry of all GCM eigenstates, whereas the  $1^+$  states belong to mixed-symmetry representations. In principle, some other high-spin many-particle states in the single- $j$  shell may also belong to the mixed-symmetry representations and will not be accessible in our implementation of the GCM. This is not a case for the  $N=8$  and  $I=2$  states in the  $j=15/2$  shell discussed here because the GCM reproduces these states exactly. On the other hand, the GCM method gives much less odd-spin states than even-spin states as compared to the exact solutions, Fig. 11. This can be understood by recalling that, for example, in the asymmetric rotor model [24] only  $(I-1)/2$  odd-spin states belong to the symmetric representation as compared to the  $I/2+1$  even-spin states. One should also stress that the standard Bohr collective quadrupole model [5] describes the symmetric states only.

Comparing the results for 10 and 19 points, Fig. 11, we may see that only three collective  $I=3$  states are found in our GCM space in the former case. The lowest one clearly reproduces the lowest exact state while the first-excited state is probably fragmented among three excited exact solutions. For 19 points 7 states are found of which the lowest 4 correspond to the exact ones. For  $I=5$  only two collective states are found; the third excited state appears for 19 points at the correct energy, but it is absent in the 10 point results. Similar analysis shows that the four lowest  $I=4$  and  $I=6$  states can be considered as collective ones.

The lowest GCM states with spins up to  $I=18$  are shown in Fig. 12. Full circles denote states with positive signature  $(-1)^I$  and open circles with the negative signature. The states are connected by lines according to their stretched E2 matrix elements, see Sec. II A. In order to illustrate the convergence properties of the GCM we draw such lines only between states which have the GCM absolute energies precise to better than 3.5% as compared with the exact values. Again we see that the 10-point GCM calculation selects two lowest collective bands while in the 19-point results many higher excited, and not necessarily collective states are found.

## B. GCM solutions for $j=31/2$

In Fig. 13 we show the GCM energies for  $I=0$  states of  $N=8$  particles obtained for different values of the cut-off parameter  $k$ . The vertical dashed lines are placed between the results obtained with  $k=k_{\text{crit}}$  and  $k=k_{\text{crit}}+1$  to show the values of the critical cut-off parameters  $k_{\text{crit}}$  determined as described in Sec. IV A. For the 10-point mesh in the intrinsic frame of reference, Fig. 13(a), we obtain the two lowest  $I=0$  states for  $k=1$  and 2, respectively. Only the first of them has a fairly correct energy already for  $k=1$ ; the energy of the second one decreases rapidly and stabilizes around  $k=6$ . According to our method of identifying collective states, the third and probably the fourth collective  $I=0$  states appear at  $k=3$  and 5, respectively, and then become strongly fragmented. This picture is confirmed by the 19-point results presented in Fig. 13(b).

A similar analysis of the  $I=2$  states, Fig. 14, shows that the lowest three of them have a collective nature while other three collective structures (appearing at  $k=4, 8,$  and  $11$  in Fig. 14(b)) become completely mixed and disappear in the dense non-collective spectrum.

Figs. 15(a-f) show the GCM spectra for particle numbers  $N=4$  to  $N=14$ , respectively, obtained by using the 19-point mesh of intrinsic deformations. All presented GCM eigenenergies correspond to states fulfilling the criterion of stability with respect to the cut-off parameters  $k \leq k_{\text{crit}}$  as well as have correct average values of  $\langle \hat{I}^2 \rangle$ ,  $\langle \hat{N} \rangle$ ,  $\langle \hat{N}^2 \rangle$ , and  $\langle \hat{H} \rangle$ , as discussed in Sec. IV A.

The spectrum for  $N=4$  can be compared with the exact results shown in Fig. 6. It is seen that the lowest GCM collective bands agree very well with the exact calculations. This is due to the fact that the dimension of the Hilbert space is here not too large and the GCM generating functions seem to exhaust it, at least for lower spins. The states for spins higher than  $I=12$  are reproduced less accurately and the bands gradually disappear, even if in the exact results they can be followed up to still higher spins. The bending up at higher spins of the  $n_\gamma=2$  GCM bands illustrates the effect of decreasing possibility of the GCM states to exhaust the exact Hilbert space.

For all particle numbers one may clearly distinguish at least five lowest collective bands. All of them are similar to those for  $N=4$  and may accordingly be interpreted as the  $\gamma$  vibrations coupled to an axial rotor, see Sec. II A. In all these cases one cannot see any candidate for low-energy  $\beta$  vibrations [23].

With an increasing particle number the GCM collective quadrupole bands lose their regularity. This effect can probably be attributed to a decreasing ability of the generating functions used in this study to exhaust the space of quadrupole collective excitations. But even for  $N=14$  the low-energy collective bands are visible. On the other hand, for the  $\gamma$ -unstable case corresponding to the half-filled shell ( $N=16$ ), we could not obtain any stable GCM solutions even by using the 19-point mesh of generating coordinates.

## V. SUMMARY AND CONCLUSIONS

In the present paper we have discussed properties of states of particles moving in a single- $j$  shell and interacting with the quadrupole-quadrupole force. This system exhibits collective as well as non-collective features and we have analyzed a possibility to select the collective subspace by using the generator coordinate method (GCM).

The GCM generating functions have been constructed as coherent excitations built from the single-particle quadrupole operator. This type of building blocks has been proposed in the single-particle coherent excitation model (SCEM) which constitutes an interesting alternative to other models based on a building-block concept, e.g., the bosonic IBM model [25] and the algebraic Ginocchio models [40]. A collective model constructed in this way is based on purely fermionic objects and requires no closed algebraic properties.

Depending on the number of different intrinsic-state configurations used in the GCM we obtain different precision of results as compared with exact solutions. When this number is relatively small, the GCM is shown to correctly select the quadrupole collective structures, while when this number is large all exact states are obtained with high precision.

We have shown that in the single- $j$  shell the low-lying quadrupole collective states can be interpreted in the frame of a standard geometrical collective model, either in its limit of an axial rotor coupled to  $\gamma$ -vibrations or in the limit of a  $\gamma$ -unstable motion. In the single- $j$  shell we did not find collective bands of the beta-vibrational character, even for  $j$  as large as  $31/2$ .

This research was supported in part by the Polish State Committee for Scientific Research under Contract No. 20450 91 01. Numerical calculations were performed at The Pittsburgh Super Computer Center under grant No. PHY900027P and at The Interdisciplinary Centre for Mathematical and Computational Modeling (ICM) of Warsaw University.

## APPENDIX A: CANONICAL BASIS FOR TRANSITION MATRIX ELEMENTS

Canonical basis for antisymmetric matrices has been introduced in Refs. [41,42] and, together with the Wick [29,5] and Onishi [43,3,5] theorems, can be used to facilitate calculation of average values of fermion operators in quasiparticle states. Here we extend the concept of the canonical basis to non-diagonal (transition) matrix elements.

We begin by considering the eigen-equation for the product of two complex antisymmetric matrices  $C^+$  and  $C'$

$$(C^+C')W = WD, \quad (\text{A1})$$

where the columns of the matrix  $W$  are linearly independent vectors of the Jordan basis, and  $D$  is the Jordan block matrix with the eigenvalues  $D_i$  at the main diagonal, the zeros or ones just above the main diagonal, and zeros elsewhere. In general, the eigenvalues  $D_i$  are complex.

Multiplying from the left-hand and right-hand sides the eigen-equation (A1) by  $W^{-1}$  and then transposing, we obtain that

$$C'(C^+W^{-1T}) = W^{-1T}D^T, \quad (\text{A2})$$

which multiplied by  $C^+$  from the left-hand side gives

$$(C^+C')(C^+W^{-1T}) = (C^+W^{-1T})D^T. \quad (\text{A3})$$

We may now discuss several specific cases depending on the degeneracy of eigenvalues.

### 1. Non-degenerate eigenvalues

Suppose that the  $i$ -th eigenvalue is non-degenerate. Then the  $i$ -th column of the matrix  $C^+W^{-1T}$  is proportional to the  $i$ -th column of  $W$ ,

$$(C^+W^{-1T})_{mi} = \alpha W_{mi}, \quad (\text{A4})$$

where  $\alpha$  is a proportionality constant. We keep the notation of indices  $m$  and  $m'$  denoting the single-particle states, although the results derived here do not depend on the assumption that these states belong to the single- $j$  shell. Multiplying both sides of Eq. (A4) by  $W_{im}^{-1}$  and summing over  $m$  we obtain

$$\alpha = (W^{-1}C^+W^{-1T})_{ii}, \quad (\text{A5})$$

which gives  $\alpha=0$ , because the right-hand-side is a diagonal matrix element of an antisymmetric matrix. From Eq. (A4) we now see that the  $i$ -th column of  $C^+W^{-1T}$  is equal to zero and hence from Eq. (A2) the corresponding eigenvalue  $D_i$  is equal to zero. Therefore, there can be at most one non-degenerate eigenvalue and it must be equal to zero. All other eigenvalues must be at least pairwise degenerate.



## 2. Doubly degenerate eigenvalues with one eigenvector

Suppose now that the matrix  $C^+C'$  has a doubly degenerate eigenvalue  $D_i$  for which only one eigenvector exists, and let this eigenvector be equal to the  $i$ -th column of  $W$ . Let the  $\tilde{i}$ -th column of  $W$  contains its partner in the  $2 \times 2$  Jordan block corresponding to this doubly degenerate eigenvalue. From (A1) we then have

$$(C^+C'W)_{mi} = D_i W_{mi}, \quad (\text{A6a})$$

$$(C^+C'W)_{m\tilde{i}} = D_i W_{m\tilde{i}} + W_{mi}, \quad (\text{A6b})$$

and from (A4),

$$[(C^+C')(C^+W^{-1T})]_{m\tilde{i}} = D_i (C^+W^{-1T})_{m\tilde{i}}, \quad (\text{A7a})$$

$$[(C^+C')(C^+W^{-1T})]_{mi} = D_i (C^+W^{-1T})_{mi} + (C^+W^{-1T})_{m\tilde{i}}. \quad (\text{A7b})$$

Comparing Eqs. (A6a) and (A7a) we see that the  $\tilde{i}$ -th column of  $C^+W^{-1T}$  must be proportional to the  $i$ -th column of  $W$ ,

$$(C^+W^{-1T})_{m\tilde{i}} = \alpha W_{mi}, \quad (\text{A8a})$$

while multiplying Eqs. (A6b) by  $\alpha$  and subtracting from (A7b) we obtain that

$$(C^+W^{-1T})_{mi} = \alpha W_{m\tilde{i}} + \beta W_{mi}, \quad (\text{A8b})$$

where  $\alpha$  and  $\beta$  are constants. However, summing Eq. (A8b) with  $W_{mi}^{-1}$  we obtain  $\beta=0$ . Similarly summing Eqs. (A8a) and (A8b) with  $W_{mi}^{-1}$  and  $W_{m\tilde{i}}^{-1}$ , respectively, we obtain that  $\alpha$  is simultaneously equal to both transposed matrix elements of an antisymmetric matrix, and hence  $\alpha=0$  too. Finally, both vectors at the left-hand sides of Eqs. (A8a) and (A8b) vanish, which is in contradiction with Eq. (A2), where the  $D$  matrix has a non-diagonal matrix element equal to one. As a conclusion we rule out the possibility of one eigenvector existing for a doubly degenerate eigenvalue. Similar derivation can be repeated for higher degeneracies and we conclude that the matrix  $D$  is always diagonal, i.e., the number of eigenvalues of the non-hermitian matrix  $C^+C'$  equals to the number of dimensions.

## 3. Doubly degenerate eigenvalue with two eigenvectors

Now we have to again consider the case of the double degeneracy and analyze the structure of the two corresponding eigenvectors. Let these eigenvectors be equal to the  $i$ -th and  $\tilde{i}$  columns of the matrix  $W$ . Similarly as in Sec. A 1 we show that the  $i$ -th and  $\tilde{i}$ -th columns of the matrix  $C^+W^{-1T}$  are also eigenvectors with the same eigenvalue and therefore must be linear combinations of the type:

$$(C^+W^{-1T})_{mi} = \alpha W_{mi} + \beta W_{m\tilde{i}}, \quad (\text{A9a})$$

$$(C^+W^{-1T})_{m\tilde{i}} = \gamma W_{mi} + \delta W_{m\tilde{i}}, \quad (\text{A9b})$$

where  $\alpha$ ,  $\beta$ ,  $\gamma$ , and  $\delta$  are constants. Summing Eqs. (A9a) and (A9b) with  $W^{-1T}_{mi}$  and  $W^{-1T}_{m\tilde{i}}$  we obtain that  $\alpha=0$  and  $\delta=0$ , respectively, while performing the summation with these factors reversed we obtain that  $\beta=-\gamma$ .

Similar procedure can be repeated for higher degeneracies with the same result that the eigenvectors of the matrix  $C^+C'$  are grouped in degenerate pairs, and that these pairs transform the  $C^+$  matrix to its canonical form where it has the form of  $2\times 2$  antisymmetric blocks with zeros elsewhere. Therefore, this canonical form can be written as

$$\left(W^{-1}C^+W^{-1T}\right)_{j\tilde{i}} = s_j c_j^* \delta_{j\tilde{i}}, \quad (\text{A10})$$

where we use the convention of the state  $\tilde{i}$  being a partner of the state  $i$ , while  $\tilde{\tilde{i}}\equiv i$ . The numbers  $c_i=c_{\tilde{i}}$  are canonical matrix elements of the matrix  $C^+$  while  $s_i=-s_{\tilde{i}}$  are the phase factors,  $|s_i|^2=1$ , depending on the phase convention chosen for the canonical matrix elements  $c_i$  and on the phases of columns of the matrix  $W$ .

Comparing Eqs. (A1) and (A10) we see that the same matrix  $W$  simultaneously transforms the second antisymmetric matrix  $C'$  to its canonical form

$$\left(W^T C' W\right)_{j\tilde{i}} = s_i^* c'_i \delta_{j\tilde{i}}, \quad (\text{A11})$$

where the canonical matrix elements  $c'_i$  of  $C'$  are related to the canonical matrix elements  $c_i^*$  of  $C^+$  by

$$c_i^* c'_i = D_i. \quad (\text{A12})$$

Since the numbers  $c_i$  depend on the normalization of columns of  $W$ , we may chose to work with the canonical basis for which  $c_i=1$  and  $c'_i=D_i$ . However, a better choice is to use the normalization in which  $c_i^*$  and  $c'_i$  are equal:

$$c_i^* = c'_i = \sqrt{D_i}, \quad (\text{A13})$$

with an arbitrary branch of the square root calculated for complex numbers  $D_i$ .

## APPENDIX B: TRANSITION MATRIX ELEMENTS IN THE CANONICAL BASIS

The Wick theorem allows to express non-diagonal matrix elements of fermion operators between the Thouless states (2.10) through three transition density matrices [5],

$$\rho_{mm'} \equiv \frac{\langle C' | a_m^+ a_m | C \rangle}{\langle C' | C \rangle} = \left[ (1 + C^+ C')^{-1} C^+ C' \right]_{mm'} , \quad (\text{B1a})$$

$$\kappa_{mm'} \equiv \frac{\langle C' | a_m a_m^+ | C \rangle}{\langle C' | C \rangle} = \left[ (1 + C^+ C')^{-1} C^+ \right]_{mm'} , \quad (\text{B1b})$$

$$\kappa'^+_{mm'} \equiv \frac{\langle C' | a_m^+ a_m^+ | C \rangle}{\langle C' | C \rangle} = \left[ C' (1 + C^+ C')^{-1} \right]_{mm'} . \quad (\text{B1c})$$

Using the canonical forms of the Thouless matrices  $C^+$  and  $C'$ , Eqs. (A10) and (A11), we obtain the transition density matrices in the canonical basis:

$$\bar{\rho}_{ji} \equiv (W^{-1}\rho W)_{ji} = \frac{D_j \delta_{ji}}{1 + D_j}, \quad (\text{B2a})$$

$$\bar{\kappa}_{ji} \equiv (W^{-1}\kappa W^{-1T})_{ji} = \frac{s_j \sqrt{D_j} \delta_{j\bar{i}}}{1 + D_j}, \quad (\text{B2b})$$

$$\bar{\kappa}'_{ji} \equiv (W^T \kappa' W)_{ji} = \frac{s_i^* \sqrt{D_i} \delta_{j\bar{i}}}{1 + D_i}, \quad (\text{B2c})$$

where the normalization (A13) was used. We see that in the canonical basis the pairing-tensor densities are related by  $\bar{\kappa} = -\bar{\kappa}'^+$ , provided phases are chosen in such a way that the phase factors  $s_i$  are real.

We may now express transition matrix elements of fermion operators through their single-particle matrix elements in the canonical basis. For the one-body and the pair-transfer operators

$$\hat{Q} = \sum_{mm'} Q_{mm'} a_m^+ a_{m'}, \quad (\text{B3a})$$

$$\hat{Q}^+ = \sum_{mm'} Q_{mm'}^+ a_m^+ a_{m'}, \quad (\text{B3b})$$

$$\hat{P}^+ = \sum_{mm'} P_{mm'}^+ a_m^+ a_{m'}, \quad (\text{B3c})$$

$$\hat{P} = \sum_{mm'} P_{mm'} a_m a_{m'}, \quad (\text{B3d})$$

we have

$$\frac{\langle C' | \hat{Q} | C \rangle}{\langle C' | C \rangle} = \sum_{mm'} Q_{mm'} \rho_{m'm} = \sum_i \frac{\bar{Q}'_{ii} D_i}{1 + D_i}, \quad (\text{B4a})$$

$$\frac{\langle C' | \hat{Q}^+ | C \rangle}{\langle C' | C \rangle} = \sum_{mm'} Q_{mm'}^+ \rho_{m'm} = \sum_i \frac{\bar{Q}^+_{ii} D_i}{1 + D_i}, \quad (\text{B4b})$$

$$\frac{\langle C' | \hat{P}^+ | C \rangle}{\langle C' | C \rangle} = \sum_{mm'} P_{mm'}^+ \kappa'_{m'm} = \sum_i \frac{\bar{P}^+_{ii} s_i^* \sqrt{D_i}}{1 + D_i}, \quad (\text{B4c})$$

$$\frac{\langle C' | \hat{P} | C \rangle}{\langle C' | C \rangle} = \sum_{mm'} P_{mm'} \kappa_{m'm} = \sum_i \frac{\bar{P}'_{ii} s_i \sqrt{D_i}}{1 + D_i}, \quad (\text{B4d})$$

where only diagonal or paired matrix elements of matrices

$$\bar{Q}' = W^{-1} Q W, \quad (\text{B5a})$$

$$\bar{Q}^+ = W^{-1} Q^+ W, \quad (\text{B5b})$$

$$\bar{P}^+ = W^{-1} P^+ W^{-1T}, \quad (\text{B5c})$$

$$\bar{P}' = W^T P W, \quad (\text{B5d})$$

have to be known.

The use of the canonical basis also facilitates calculation of transition matrix elements of two-body operators. Moreover, the particle-number projection discussed in Sec. III A can

then be performed at a very low cost. This is so because the multiplication of the Thouless matrix  $C^+$  of the ket state by the gauge phase factor  $e^{2i\phi}$  does not change the canonical eigenvectors. Only the eigenvalues  $D_i$  are multiplied by  $e^{2i\phi}$ . Here we only give expressions for particle-number-projected matrix elements of separable interactions:

$$\begin{aligned} \langle C' | \hat{Q} \hat{Q}^+ \hat{P}_N | C \rangle &= \sum_{ij} \left[ \bar{Q}'_{ii} \bar{Q}^+_{jj} D_i D_j R_2^2(i, j) \right. \\ &\quad + \bar{Q}'_{ij} \bar{Q}^+_{ji} D_j R_1^2(i, j) \\ &\quad \left. + \bar{Q}'_{ij} \bar{Q}^+_{ij} s_j s_i^* \sqrt{D_i D_j} R_1^2(i, j) \right], \end{aligned} \quad (\text{B6})$$

$$\begin{aligned} \langle C' | \hat{P}^+ \hat{P} \hat{P}_N | C \rangle &= \sum_{ij} \left[ \bar{P}'_{ii} \bar{P}^+_{jj} s_i s_j^* \sqrt{D_i D_j} R_1^2(i, j) \right. \\ &\quad \left. + 2 \bar{P}'_{ij} \bar{P}^+_{ji} D_i D_j R_2^2(i, j) \right], \end{aligned} \quad (\text{B7})$$

where  $R_k^2(i, j)$  are the residues [15,5]

$$R_k^2(i, j) = \frac{1}{2\pi} \int_0^{2\pi} d\phi \frac{\langle C' | C(\phi) \rangle e^{-i(N-2k)\phi}}{(1 + D_i e^{2i\phi})(1 + D_j e^{2i\phi})}, \quad (\text{B8})$$

which can be calculated by using the discretized integrals discussed in Sec. III A. The overlap of Thouless states is given by

$$\langle C' | C(\phi) \rangle = \det \left( 1 + e^{2i\phi} C^+ C' \right)^{1/2} = \prod_{i>0} \left( 1 + D_i e^{2i\phi} \right), \quad (\text{B9})$$

where notation  $i>0$  means that only one state from every canonical pair  $(i, \tilde{i})$  is included in the product.

### APPENDIX C: MATRIX ELEMENTS BETWEEN TIME-EVEN STATES

Suppose that the Thouless states are time-even, i.e.,

$$\hat{T} | C \rangle = | C \rangle, \quad (\text{C1})$$

where  $\hat{T}$  is the antiunitary time-reversal operator, and suppose that the single-particle basis is closed with respect to the time-reversal, i.e.,

$$\hat{T} a_m^+ \hat{T}^+ = \sum_{m'} U_{mm'}^T a_{m'}^+, \quad (\text{C2a})$$

$$\hat{T} a_m \hat{T}^+ = \sum_{m'} U_{mm'}^+ a_{m'}, \quad (\text{C2b})$$

where  $U$  is a unitary antisymmetric matrix. Then the Thouless matrix  $C^+$  defining the state  $|C\rangle$  is time-even, namely,

$$C^+ = U C^T U^T. \quad (\text{C3})$$

For every antisymmetric time-even matrix such as  $C^+$  we may define the hermitian time-even matrix  $\tilde{C}$ ,

$$\tilde{C} = C^+U^* = C^*U^+ = UC^T = U^TC, \quad (\text{C4})$$

$$\tilde{C}^+ = \tilde{C}, \quad \tilde{C} = U\tilde{C}^*U^+, \quad (\text{C5})$$

which contains the same information about the Thouless state  $|C\rangle$  as the matrix  $C^+$ . Results of Appendices A and B can now be significantly simplified.

First, the matrix  $C^+C'$  defining all transitional matrix elements becomes quasihermitian,

$$C^+C' = \tilde{C}\tilde{C}' = \tilde{C}^{1/2} \left( \tilde{C}^{1/2}\tilde{C}'\tilde{C}^{1/2} \right) \tilde{C}^{-1/2}, \quad (\text{C6})$$

i.e., by a similarity transformation  $\tilde{C}^{1/2}$  can be transformed into a hermitian matrix  $\tilde{Z}$ :

$$\tilde{Z} = \tilde{C}^{1/2}\tilde{C}'\tilde{C}^{1/2}. \quad (\text{C7})$$

Therefore, all eigenvalues  $D_i$  become real numbers. (Cases when  $\tilde{C}$  is singular can be considered separately).

Second, the eigenvectors of the hermitian matrix  $\tilde{Z}$  form a unitary matrix  $V$ ,

$$\tilde{Z}V = VD, \quad (\text{C8})$$

and hence the eigenvectors of  $C^+C'$  (cf. Eq. (A1)) are given by

$$W = \tilde{C}^{1/2}V. \quad (\text{C9})$$

Third, the hermitian matrix in Eq. (C6) is time-even and therefore has eigenvalues pairwise degenerate due to the Kramers degeneracy. Therefore, only half of the eigenvectors have to be numerically calculated and the canonical pairs of Appendix A can be identified with the time-reversed pairs [32].

## REFERENCES

- [1] E. Caurier, A. P. Zucker, A. Poves, and G. Martínez-Pinedo, *Phys. Rev.* **C50**, 225 (1994).
- [2] D. L. Hill and J. A. Wheeler, *Phys. Rev.* **89**, 1102 (1953).
- [3] N. Onishi and S. Yoshida, *Nucl. Phys.* **80**, 367 (1966).
- [4] C. W. Wong, *Phys. Rep.* **15C**, 283 (1975).
- [5] P. Ring and P. Schuck, *The Nuclear Many Body Problem* (Springer-Verlag, New York, 1980).
- [6] S. T. Belyaev, *Congrès Int. de physique nucléaire* (Paris, 1958); *Mat. Fys. Medd. Dan. Vid. Selsk.* **31**, No. 11 (1959).
- [7] W. J. Mulhall and L. Sips, *Nucl. Phys.* **57**, 565 (1964).
- [8] M. Baranger and K. Kumar, *Nucl. Phys.* **62**, 113 (1965).
- [9] M. Baranger and K. Kumar, *Nucl. Phys.* **A110**, 490, 529 (1968); *Nucl. Phys.* **A122**, 244 (1968).
- [10] A. Arima, *Prog. Theor. Phys., Suppl. extra number*, 489 (1968).
- [11] M. I. Friedman and I. Kelson, *Nucl. Phys.* **A144**, 209 (1970).
- [12] J. Dobaczewski, *Phys. Lett.* **241B**, 289 (1990).
- [13] J. Dobaczewski and S.G. Rohoziński, *Proceedings of the 3rd International Spring Seminar on Nuclear Physics*, ed. A. Covello (World Scientific, Singapore, 1991) p. 351.
- [14] B. F. Bayman, *Nucl. Phys.* **15**, 33 (1960).
- [15] K. Dietrich, H. J. Mang, and J. H. Pradal, *Phys. Rev.* **135**, B22 (1964).
- [16] V. N. Fomenko, *J. Phys. A* **3**, 8 (1970).
- [17] R. A. Sorensen, *Phys. Lett.* **38B**, 376 (1972).
- [18] M. G. Redlich and E. P. Wigner, *Phys. Rev.* **95**, 122 (1954).
- [19] R. E. Peierls and J. Yoccoz, *Proc. Phys. Soc.* **A70**, 381 (1957).
- [20] Y. Tanaka, K. Ogawa, and A. Arima, *Prog. Theor. Phys.* **45**, 85 (1971).
- [21] M. Vallières and R. M. Dreizler, *Nucl. Phys.* **A175**, 272 (1971).
- [22] L. Wilets and M. Jean, *Phys. Rev.* **102**, 788 (1956).
- [23] Absence of  $\beta$  vibrations has recently been analyzed in a survey of experimental data, R. F. Casten, P. von Brentano, and N. V. Zamfir, *Phys. Rev.* **C49**, 1940 (1994), and in the interacting boson model, R. F. Casten and P. von Brentano, *Phys. Rev.* **C50**, R1280 (1994). Our results show that the same feature appears in a purely fermionic model of a single- $j$  shell.
- [24] A. Bohr and B. R. Mottelson, *Nuclear Structure* (Benjamin, New York, 1975), Vol II.
- [25] A. Arima and F. Iachello, *Phys. Rev. Lett.* **35**, 1069 (1975); *Ann. Phys. (N.Y.)* **99**, 253 (1976); *Ann. Phys. (N.Y.)* **111**, 201 (1978); *Ann. Phys. (N.Y.)* **123**, 468 (1979).
- [26] We denote the quadrupole deformation by the traditional symbol  $\beta$  but its scale does not correspond to the usual Bohr's variable. In fact, in the single- $j$  shell the quadrupole moment (and the deformation) can be scaled arbitrarily because the radial wave function is not specified.
- [27] R. Balian and E. Brezin, *Nuovo Cim.* **64B**, 37 (1969).
- [28] D. J. Thouless, *Nucl. Phys.* **21**, 225 (1960).
- [29] G. C. Wick, *Phys. Rev.* **80**, 268 (1950).
- [30] H. A. Lamme and E. Boeker, *Nucl. Phys.* **A111**, 492 (1968).
- [31] N. MacDonald, *Adv. Phys.* **19**, 371 (1970).

- [32] K. Neergård and E. Wüst, Nucl. Phys. **A402**, 311 (1983).
- [33] K. W. Schmid, F. Grümmer, and A. Faessler, Phys. Rev. C **29**, 291 (1984).
- [34] D. Baye and P.-H. Heenen, Phys. Rev. C **29**, 1056 (1984).
- [35] J. O. Corbet, Nucl. Phys. **A169**, 426 (1971).
- [36] D. A. Varshalovich, A. N. Moskalev, and V. K. Khersonkii, *Quantum Theory of Angular Momentum* (World Scientific, Singapore, 1988)
- [37] M. Abramowitz and I. A. Stegun, *Handbook of Mathematical Functions* (Dover, New York, 1965).
- [38] P. Bonche, J. Dobaczewski, H. Flocard, P.-H. Heenen, and J. Meyer, Nucl. Phys. **A510**, 466 (1990).
- [39] As shown in Ref. [38], spurious states may appear even if all eigenvalues of the overlap matrix are positive. This can be attributed to the fact that no exact particle number and angular momentum projection has been performed in that study.
- [40] J. N. Ginocchio, Phys. Lett. **79B**, 173 (1978); Ann. Phys. (N.Y.) **126**, 234 (1980).
- [41] B. Zumino, J. Math. Phys. **3**, 1055 (1962).
- [42] C. Bloch, A. Messiah, Nucl. Phys. **39**, 95 (1962).
- [43] P. O. Löwdin, Phys. Rev. **97**, 1474 (1955).

TABLES

TABLE I. Absolute values of the reduced matrix elements of the quadrupole operator between the lowest  $2^+$  and  $0^+$  states obtained in the exact calculation for  $j=15/2$  and  $N=8$ .

	$0_1^+$	$0_2^+$	$0_3^+$	$0_4^+$	$0_5^+$
$2_1^+$	1.921	0	0.017	0.003	0
$2_2^+$	0	1.307	0	0	0.014
$2_3^+$	0	1.231	0	0	0.034
$2_4^+$	0.086	0	0.790	0.208	0
$2_5^+$	0.070	0	0.387	0.437	0

TABLE II. Same as Table I for  $j=31/2$  and  $N=4$ .

	$0_1^+$	$0_2^+$	$0_3^+$	$0_4^+$
$2_1^+$	1.366	0.004	<0.001	<0.001
$2_2^+$	0.099	0.109	0.001	<0.001
$2_3^+$	0.005	1.091	0.018	0.002
$2_4^+$	0.001	0.181	0.206	0.015
$2_5^+$	<0.001	0.020	0.833	0.072



TABLE III. The decomposition of the  $N=8$  SCEM collective states (2.3) in the single- $j$  shell for  $j=15/2$  into states of good angular momentum. The numbers of new states obtained for a given value  $N_F$  as compared to those for  $N_F-1$  are listed for every  $I$ .

$I$	$N_F$									
	0	1	2	3	4	5	6	7	8	9
0	1	0	1	1	1	1	1	1	0	0
1	0	0	0	0	0	1	2	1	0	0
2	0	1	1	1	2	3	5	3	0	0
3	0	0	0	1	1	2	4	4	1	0
4	0	0	1	1	2	5	7	6	3	0
5	0	0	0	0	1	2	6	8	4	0
6	0	0	0	1	1	2	6	3	8	0
7	0	0	0	0	0	1	2	9	11	3
8	0	0	0	0	1	1	2	7	15	9
9	0	0	0	0	0	0	1	3	11	11
10	0	0	0	0	0	1	1	2	9	15
11	0	0	0	0	0	0	0	1	3	13
12	0	0	0	0	0	0	1	1	3	10
13	0	0	0	0	0	0	0	0	1	4
14	0	0	0	0	0	0	0	1	1	3
15	0	0	0	0	0	0	0	0	0	1
16	0	0	0	0	0	0	0	0	1	1
17	0	0	0	0	0	0	0	0	0	0
18	0	0	0	0	0	0	0	0	0	1

TABLE IV. Maximum quadrupole moments

$j$	$N$	$Q_{\max}$
15/2	8	1.6
31/2	10	1.7
31/2	12	2.0
31/2	14	2.2
31/2	16	2.4

TABLE V. Numbers of states  $N_{\text{exact}}$  of spin  $I$  in the single- $j$  shell for  $j=15/2$  and  $N=8$  particles compared with the numbers  $k_{\text{crit}}$  of eigenvalues of the overlap matrix retained for the 10 and 19 point GCM calculations (see text).

$I$	$N_{\text{exact}}$	$k_{\text{crit}}$ (10 points)	$k_{\text{crit}}$ (19 points)
0	7	7	7
1	4	–	–
2	16	12	16
3	13	3	7
4	25	13	21
5	21	6	12
6	31	15	22
7	26	8	14
8	35	16	24
9	29	10	16
10	35	16	23
11	29	11	15
12	34	14	18
13	27	10	11
14	30	10	11
15	23	6	6
16	25	6	6
17	19	3	3
18	20	4	4

## FIGURES

FIG. 1. Exact yrast spectra for  $N=8$  and  $j=15/2$  obtained with varying strength of pairing and quadrupole interactions.

FIG. 2. Exact yrast spectra for for different particle numbers  $N$  and shell angular momenta  $j$ .

FIG. 3. Single-particle energies in the intrinsic frame for  $j=15/2$  as functions of the quadrupole moment  $Q$  (the Nilsson diagram). Exchange term in the mean field is neglected.

FIG. 4. Potential energy surfaces (PES) as functions of the  $\beta$ - $\gamma$  collective coordinates corresponding to  $j=15/2$  and  $N=8$  (a), and to  $j=31/2$  and  $N=10$  (b). Full dots denote 10 deformation points used in discretizing the GCM equation in the intrinsic frame.

FIG. 5. Exact spectrum for  $N=8$  particles occupying the  $j=15/2$  shell

FIG. 6. Exact spectrum for  $N=4$  particles occupying the  $j=31/2$  shell

FIG. 7. CPU times required to calculate one hundred of overlaps for different Euler angles as a function of the shell angular momentum  $j$ . Solid lines show polynomial fits to the PC-486 and CRAY results,  $0.237j^3 + 0.882j^2$  and  $0.159j^2 + 0.314j$ , respectively.

FIG. 8. Absolute values of eigenvalues of the GCM overlap matrix for  $j=15/2$  and  $N=8$ . Results obtained with the 19-point mesh are shown for  $I=0$  (a) and  $I=6$  (b).

FIG. 9. GCM spectra of spin  $I=0$  states obtained for different values of the cut-off parameter  $k$ . Results obtained with 10 (a) and 19 (b) mesh points of intrinsic deformations are shown for  $j=15/2$  and  $N=8$ .

FIG. 10. Same as Fig. 9 for the  $I=2$  states.

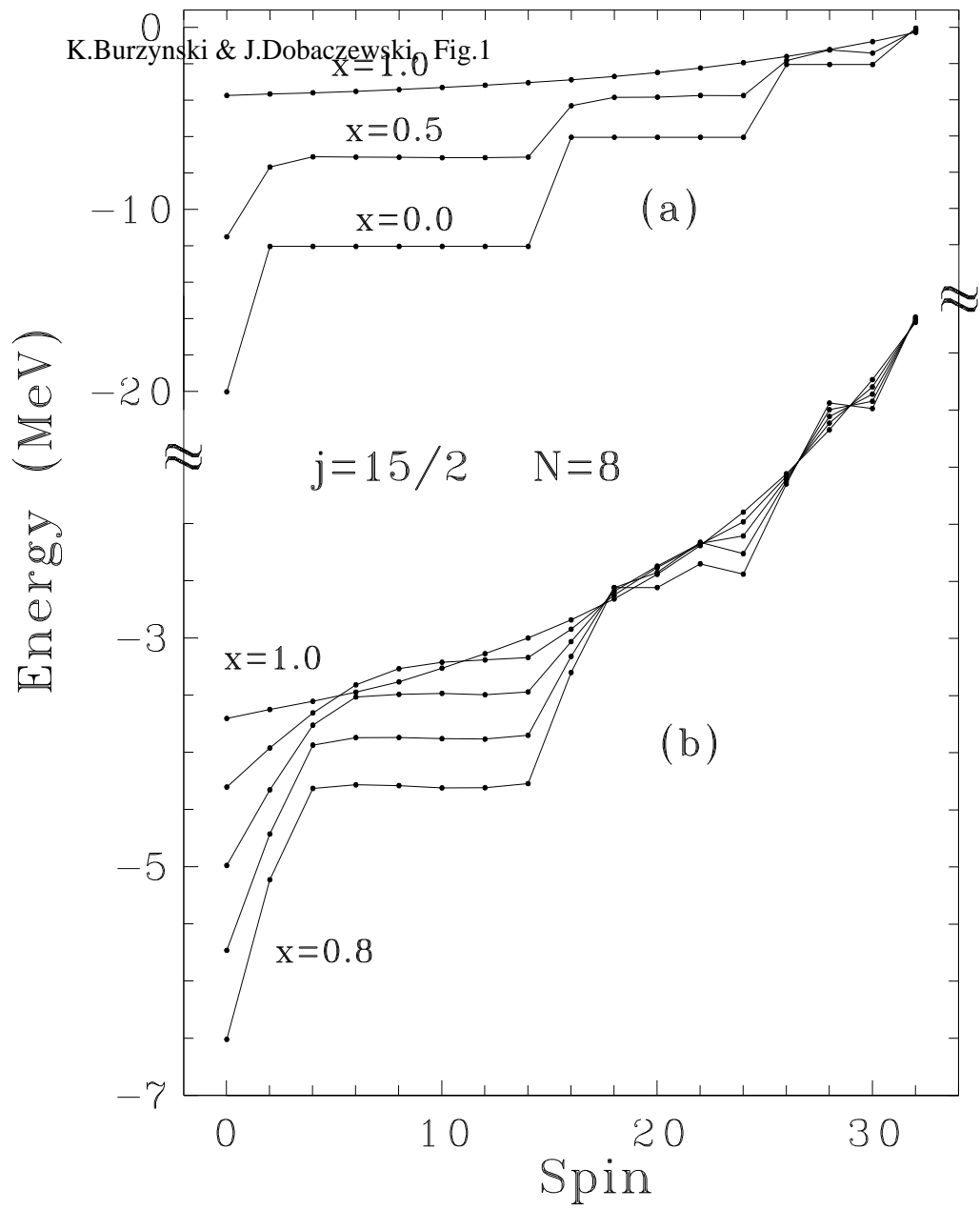
FIG. 11. GCM spectra of low-spin spin  $I \leq 6$  states obtained with 10 (a) and 19 (b) mesh points of intrinsic deformations shown for  $j=15/2$  and  $N=8$ .

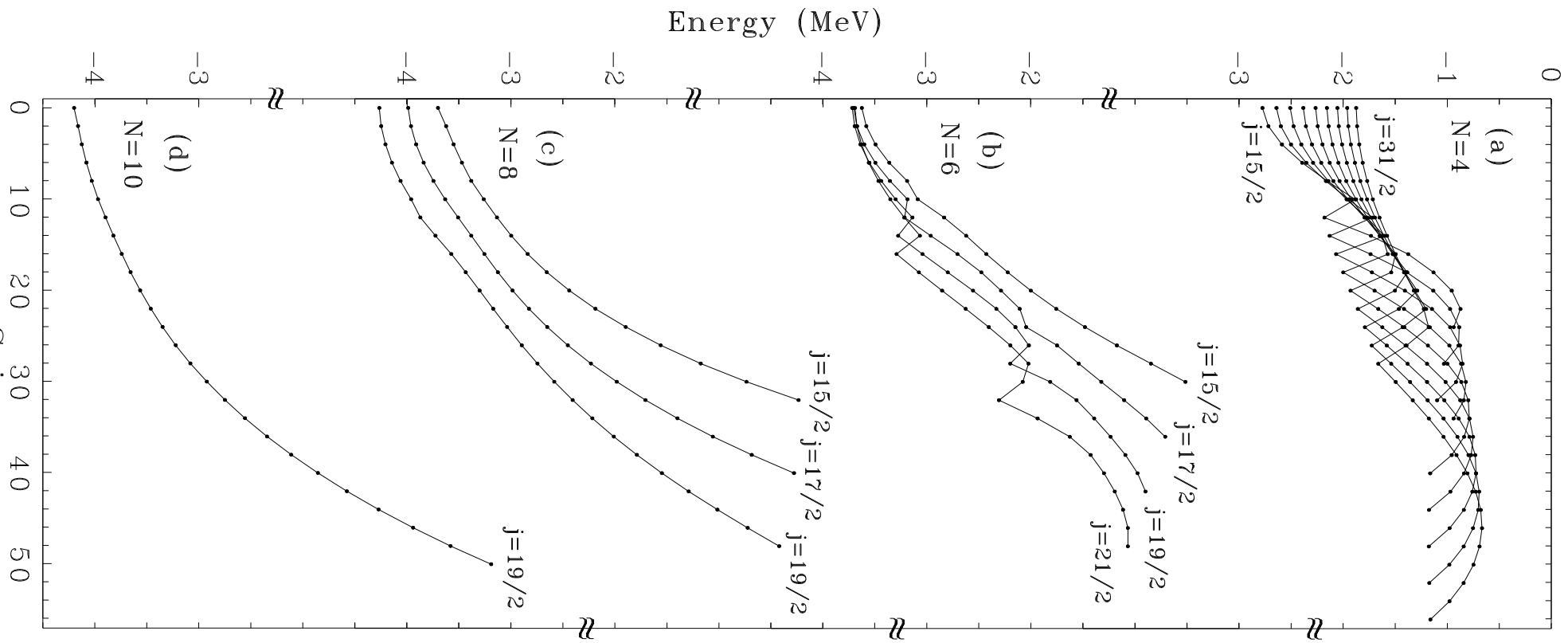
FIG. 12. GCM spectra of low-energy spin  $I \leq 18$  states obtained with 10 (a) and 19 (b) mesh points of intrinsic deformations shown for  $j=15/2$  and  $N=8$ .

FIG. 13. Same as Fig. 9 for  $j=31/2$  and  $N=10$ .

FIG. 14. Same as Fig. 10 for  $j=31/2$  and  $N=10$ .

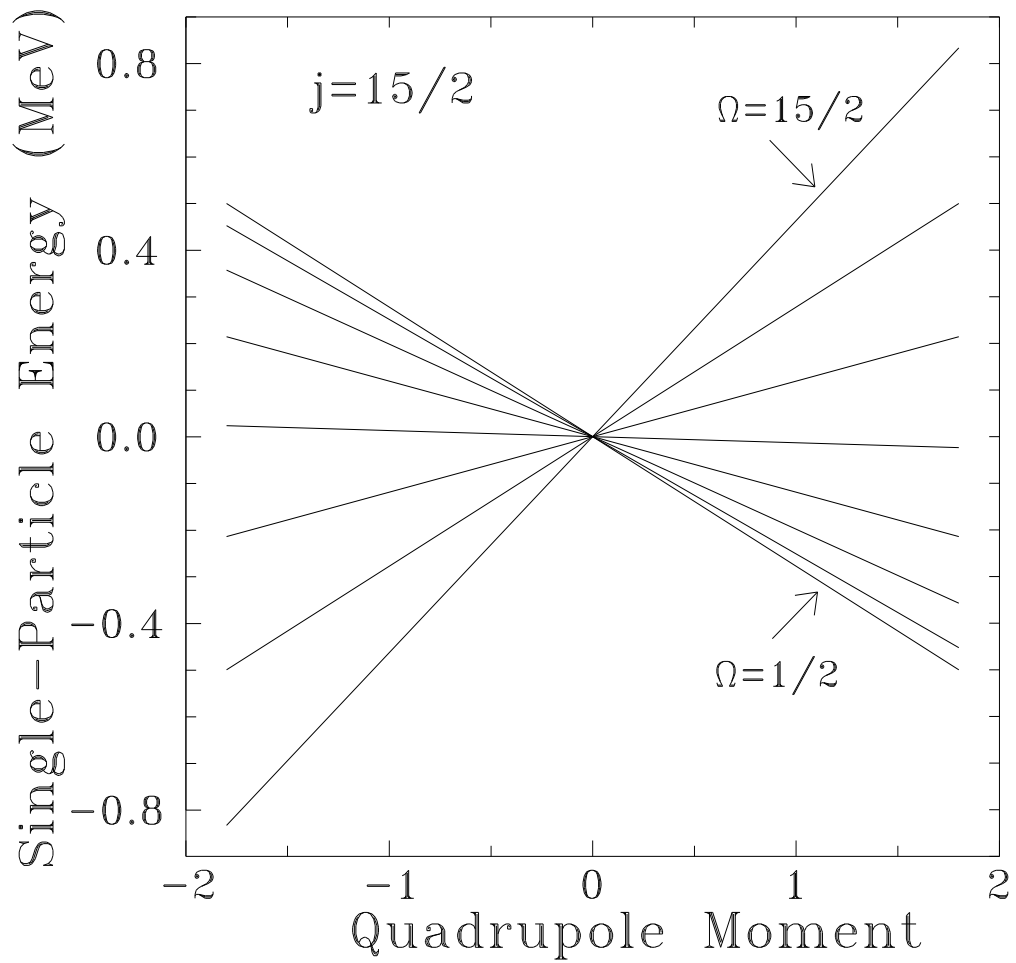
FIG. 15. GCM spectra for  $j=31/2$  obtained with 19 mesh points of intrinsic deformations for particle numbers between  $N=4$  and  $N=14$ , (a) to (f), respectively.

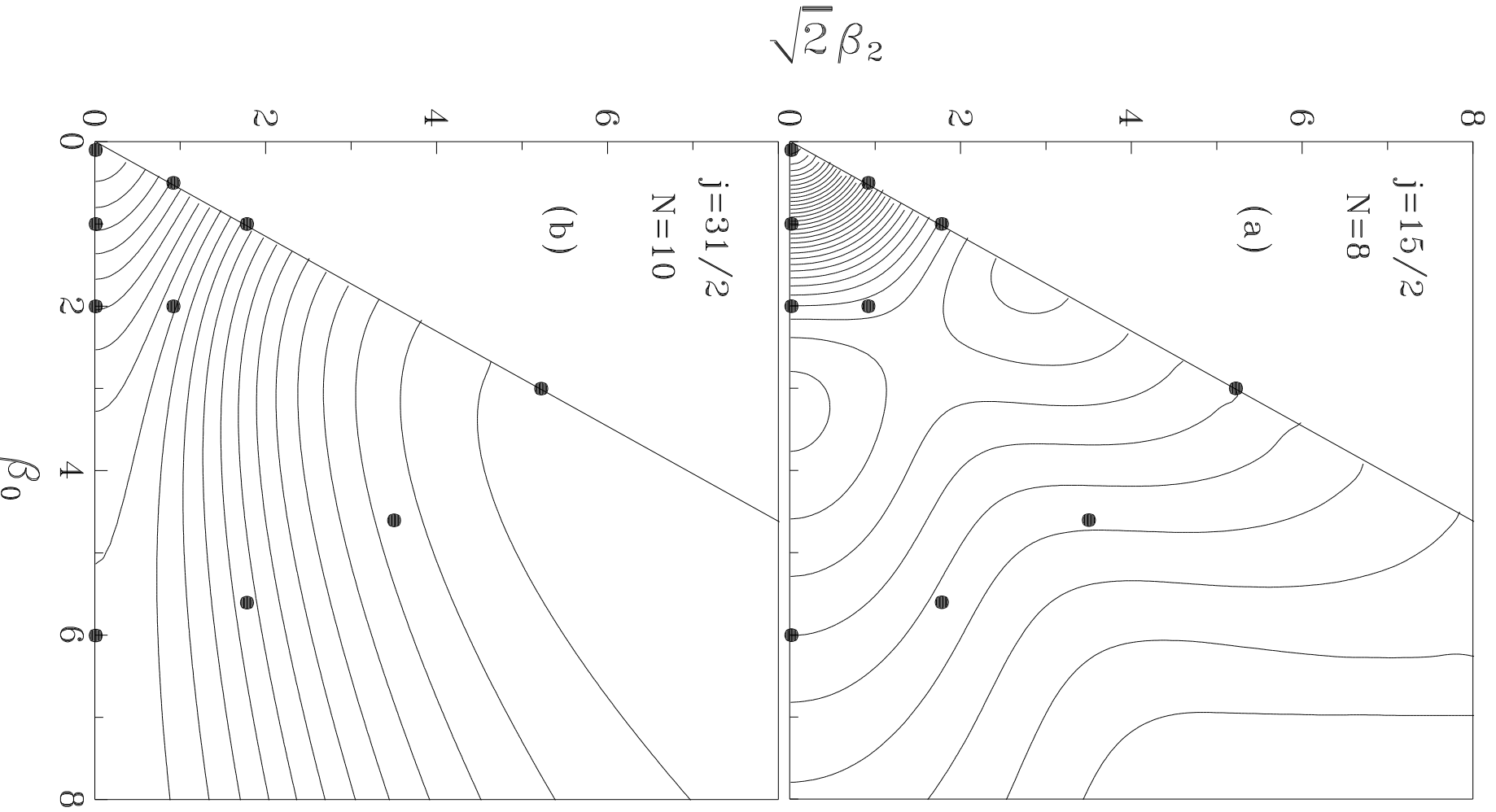




K.Burzynski & J.Dobaczewski, Fig.2

K.Burzynski & J.Dobaczewski, Fig.3

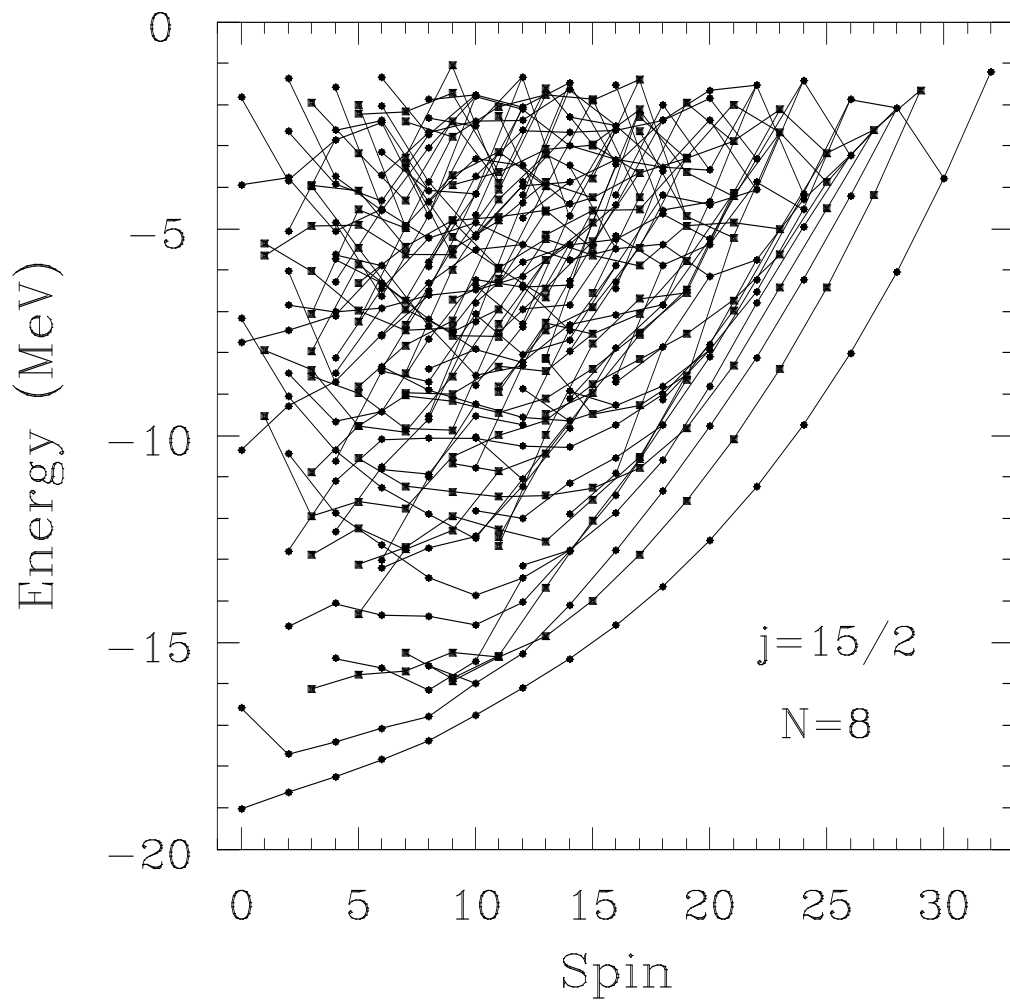




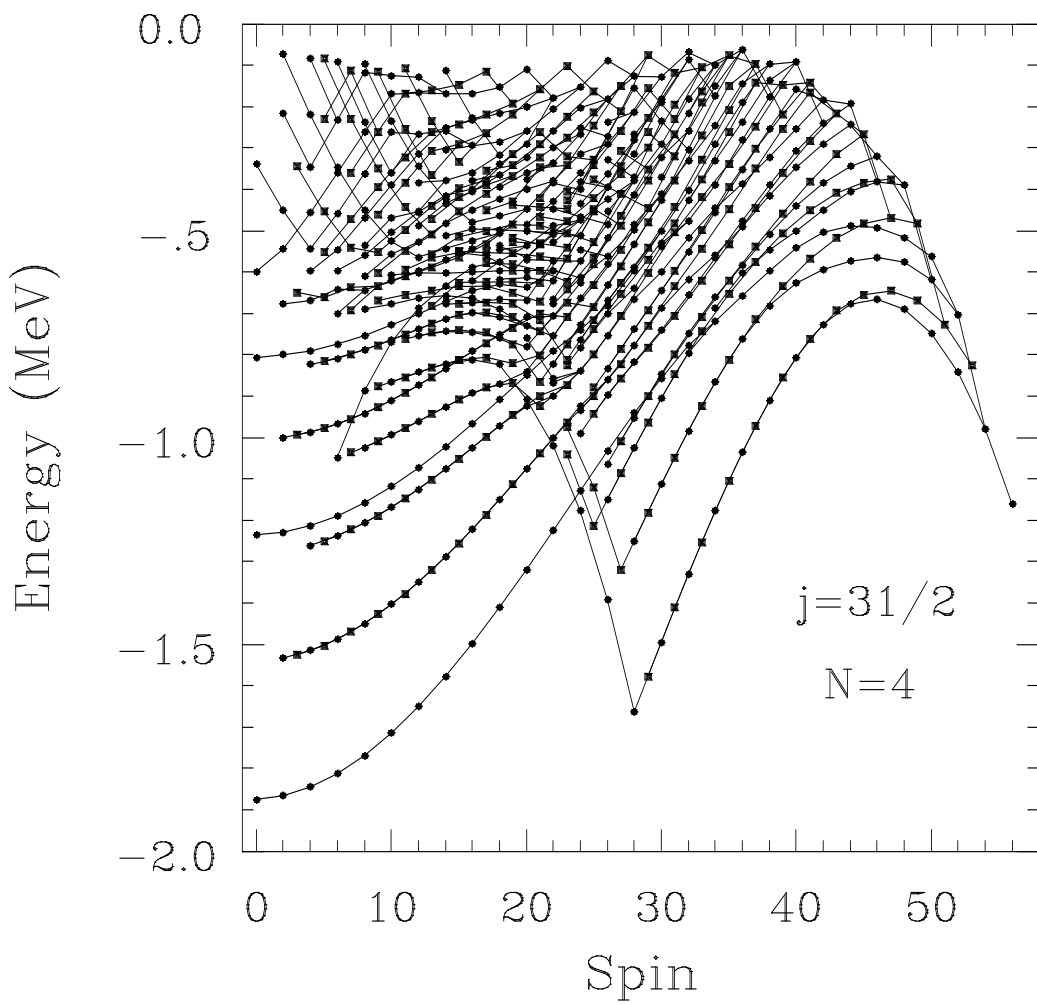
K.Burzynski & J.Dobaczewski, Fig.4



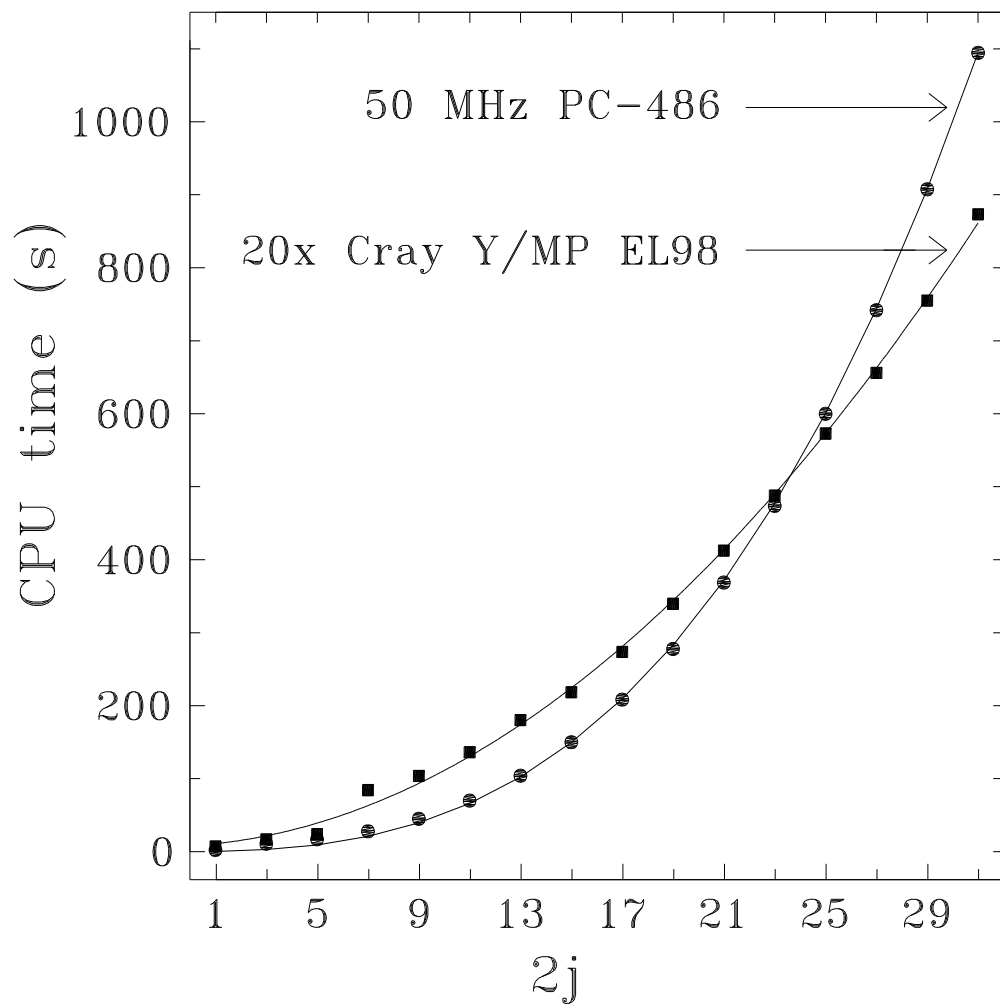
K.Burzynski & J.Dobaczewski, Fig.5

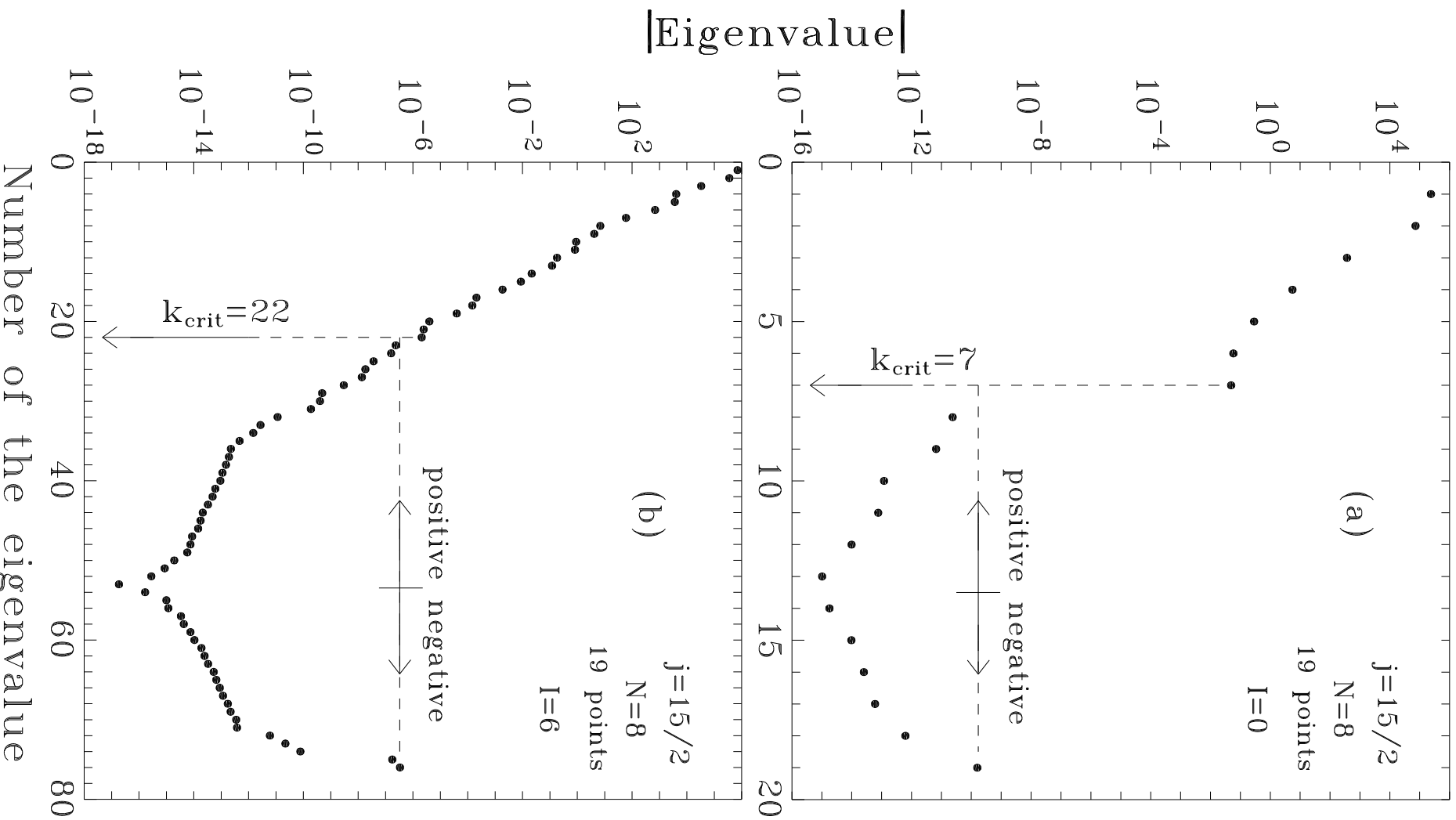


K.Burzynski & J.Dobaczewski, Fig.6



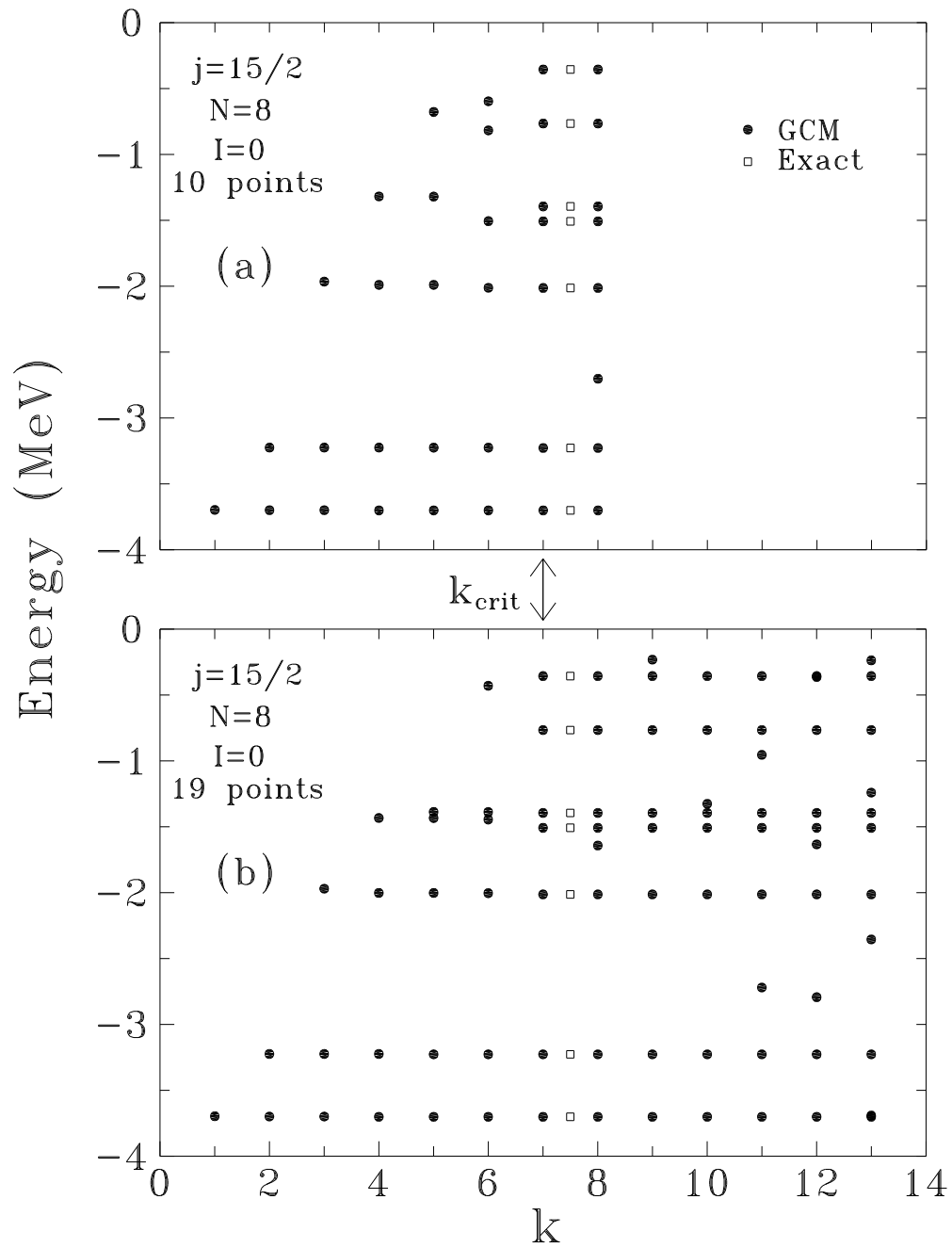
K.Burzynski & J.Dobaczewski, Fig.7



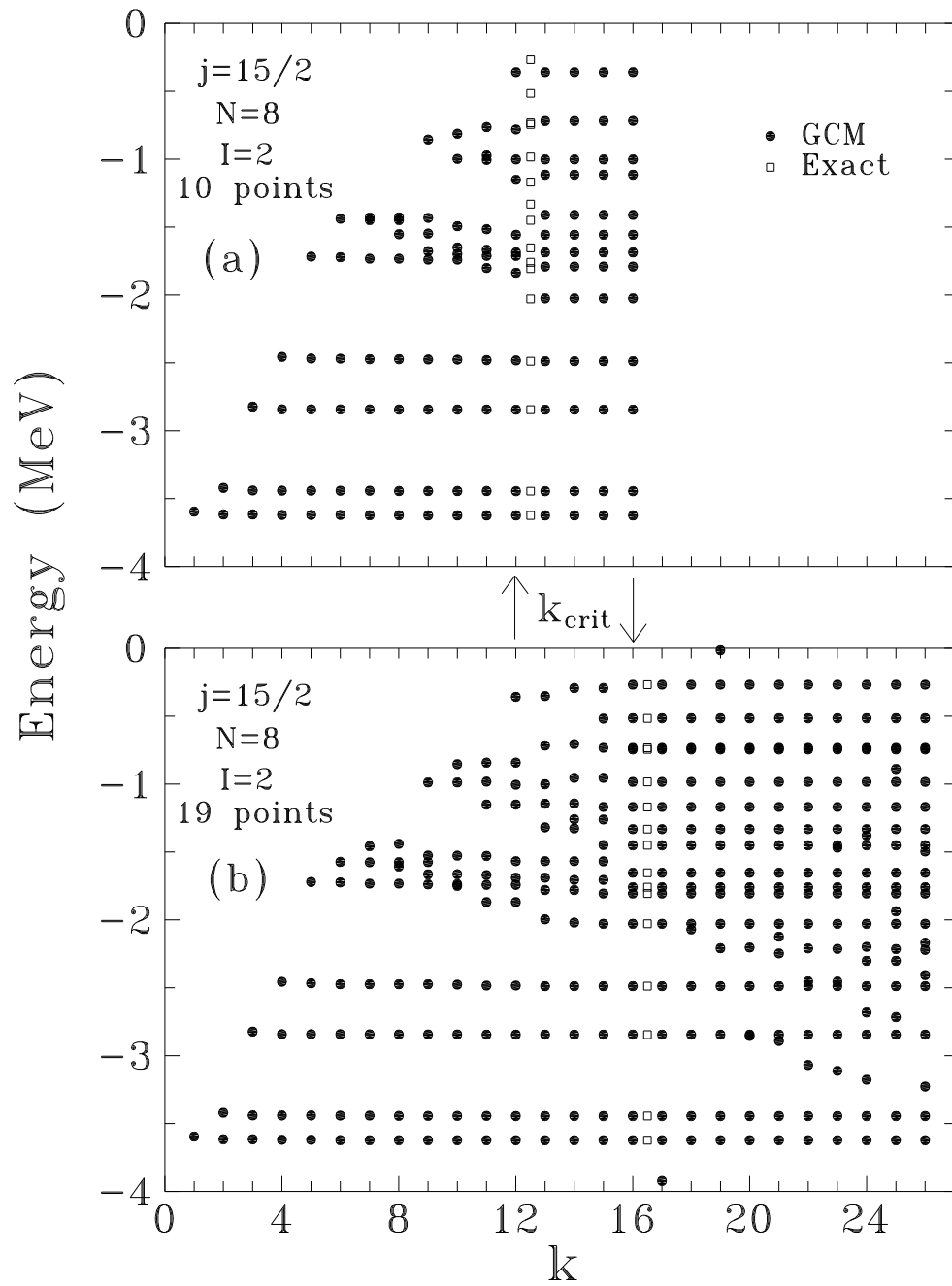


K.Burzynski & J.Dobaczewski, Fig.8

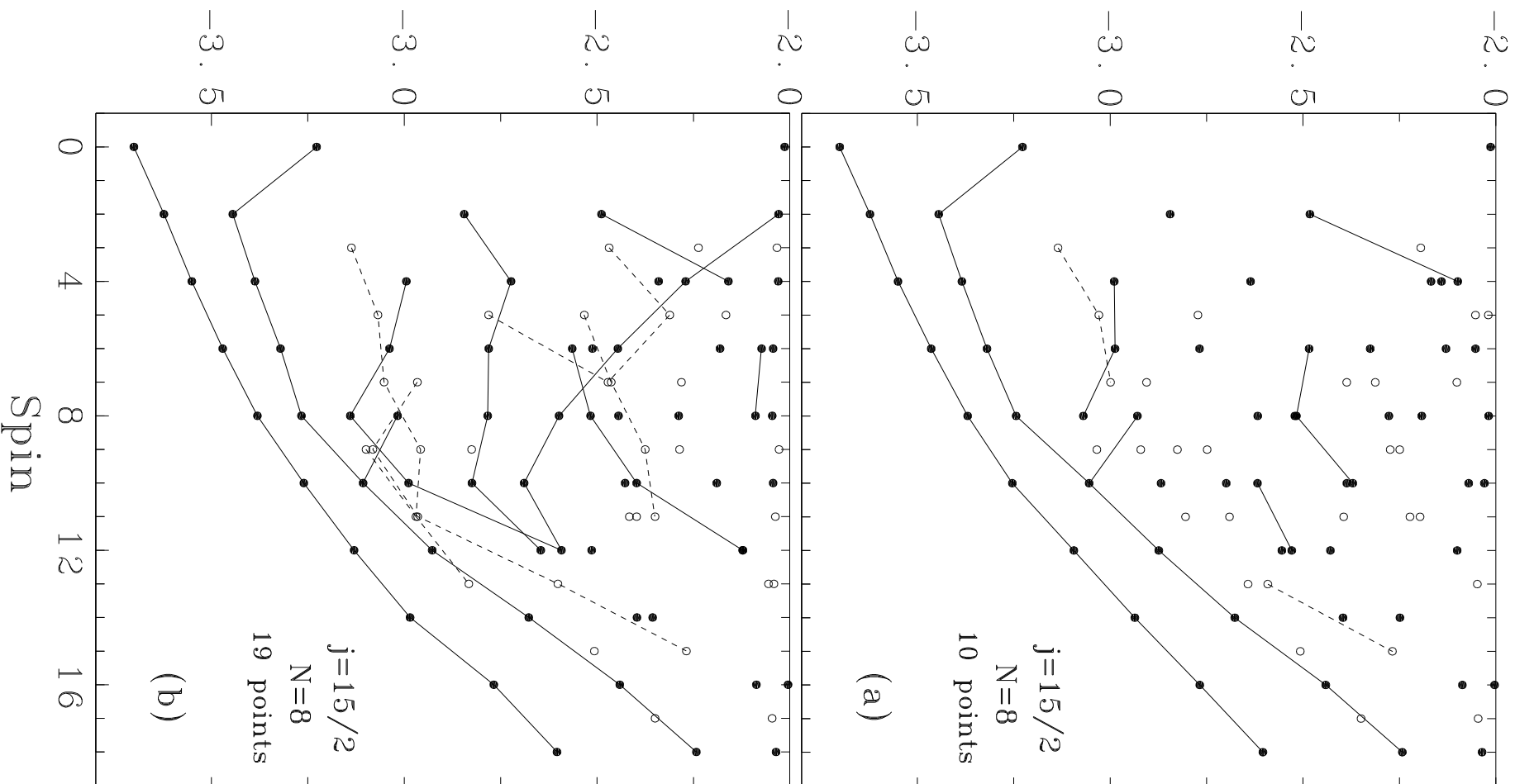
K.Burzynski & J.Dobaczewski, Fig.9



K.Burzynski & J.Dobaczewski, Fig.10

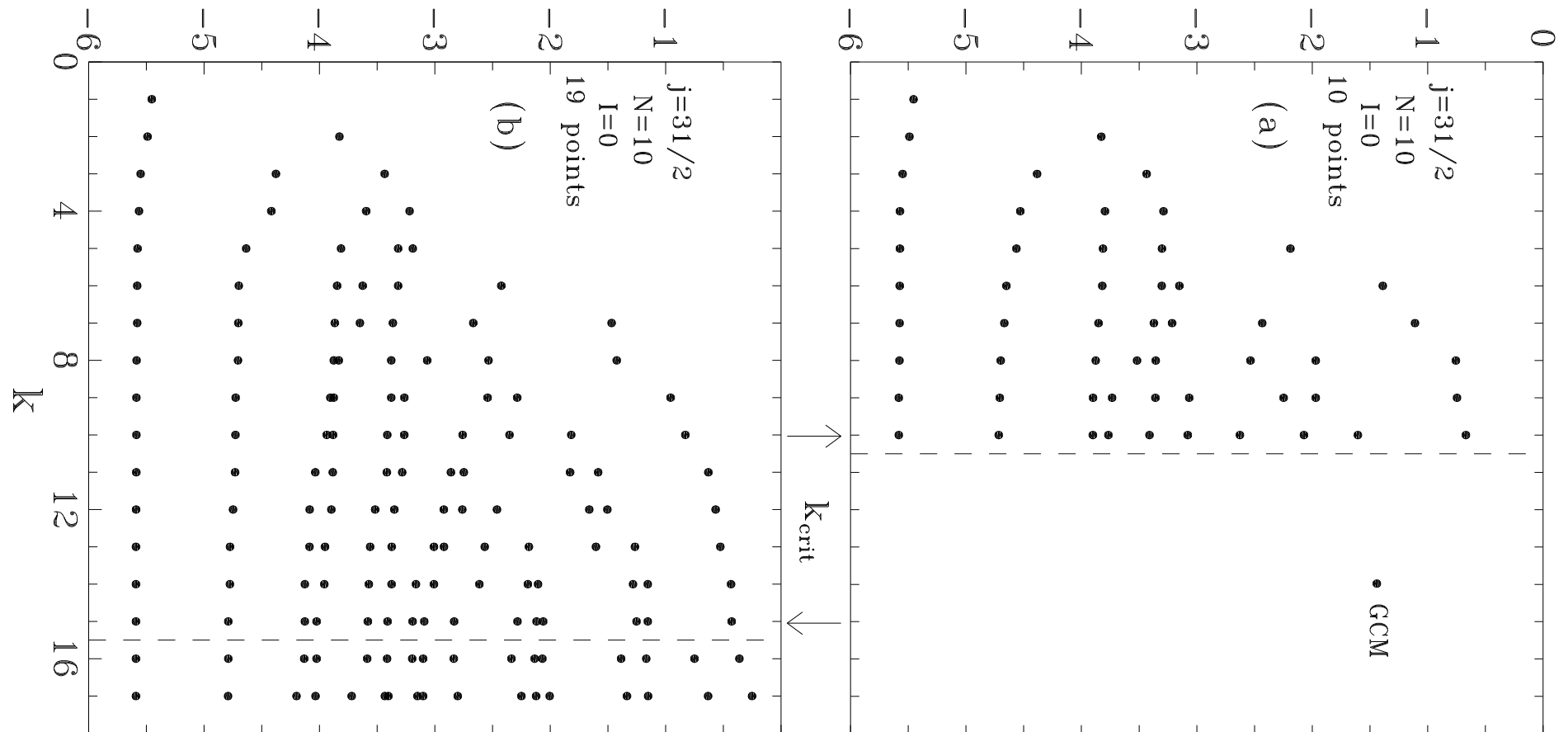


Energy (MeV)



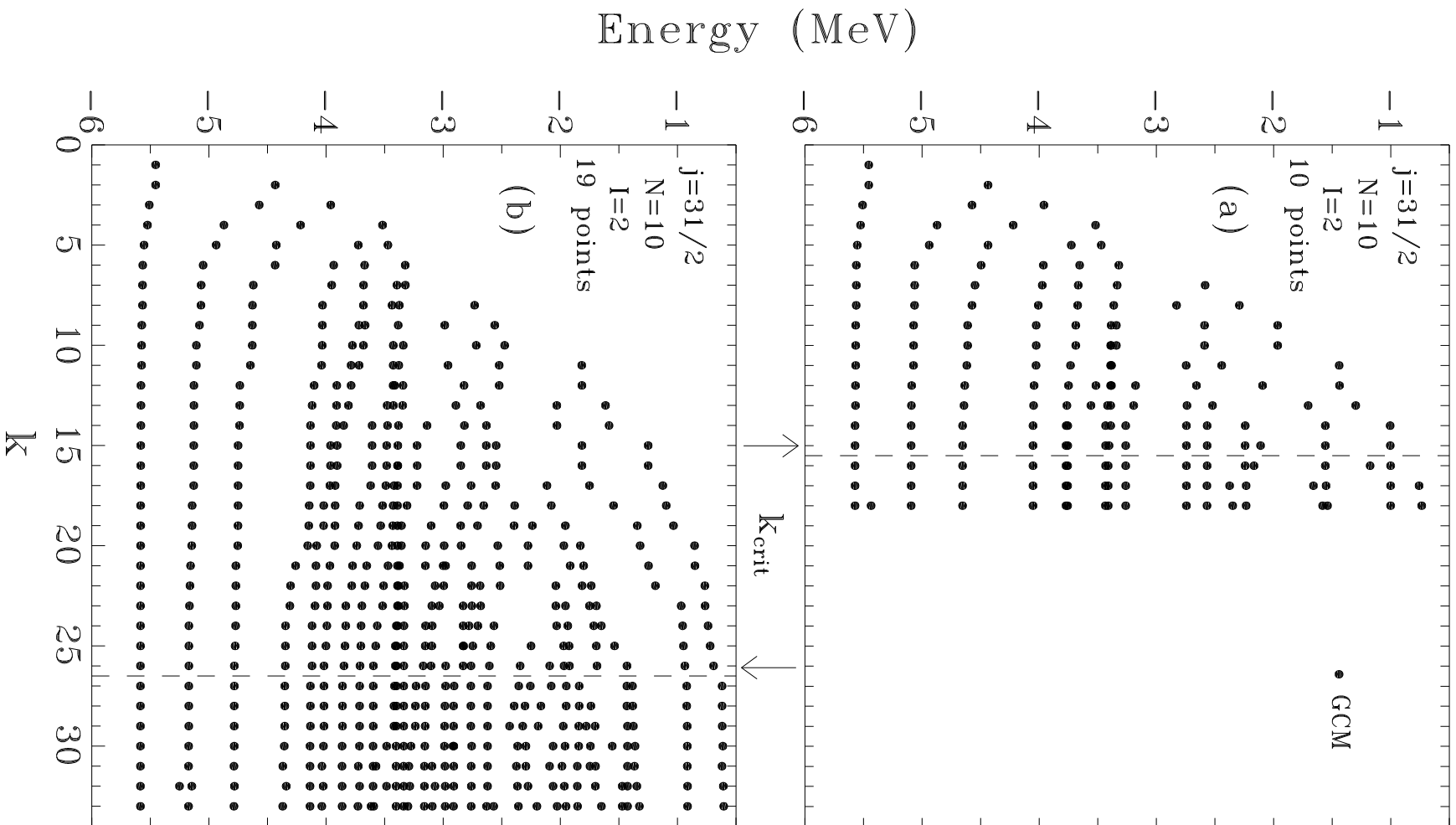
K.Burzynski & J.Dobaczewski, Fig.12

Energy (MeV)



K.Burzynski & J.Dobaczewski, Fig.13





K.Burzynski & J.Dobaczewski, Fig.14

